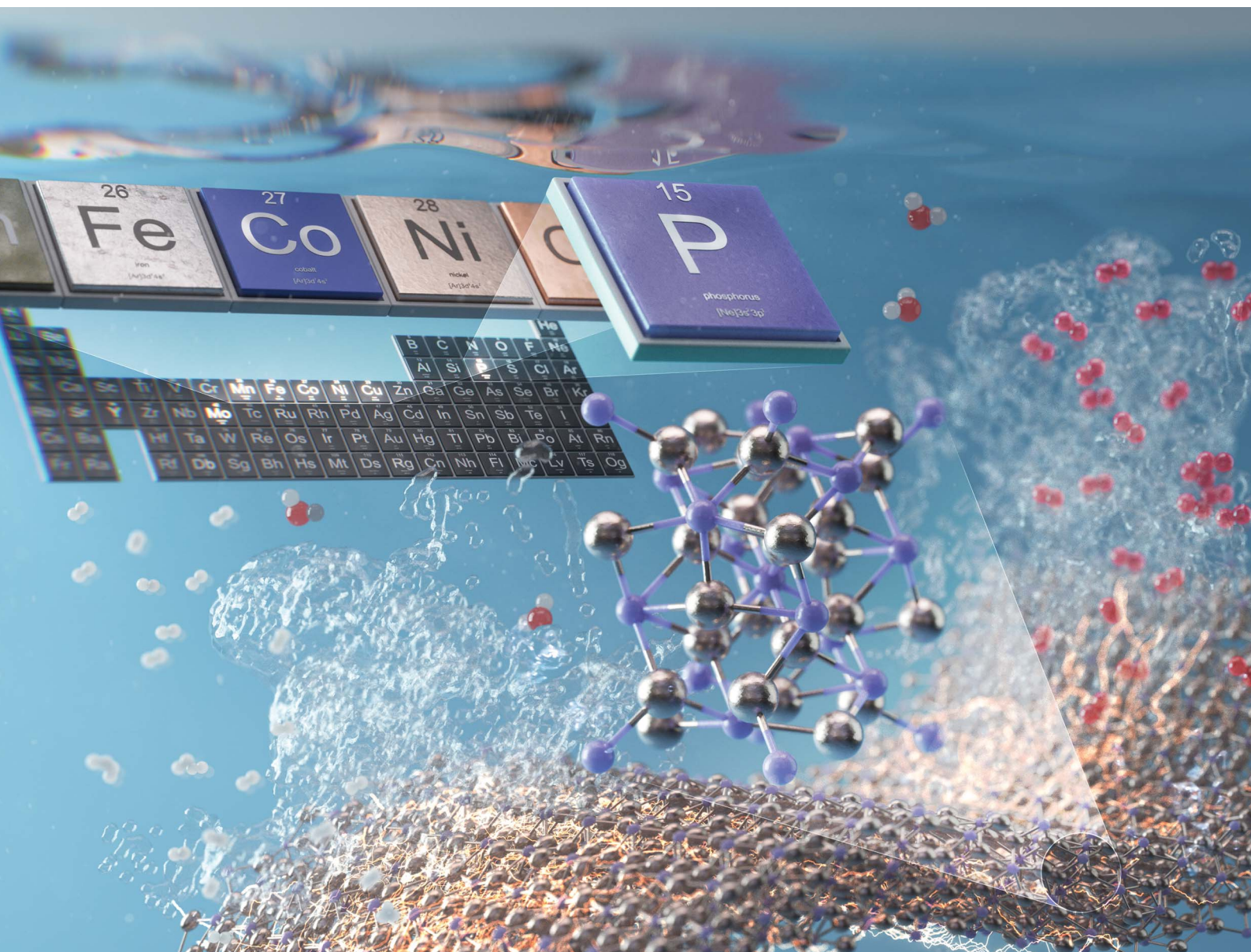


Journal of Materials Chemistry A

Materials for energy and sustainability

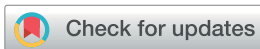
rsc.li/materials-a



ISSN 2050-7488

REVIEW ARTICLE

Don-Hyung Ha *et al.*
Basics, developments, and strategies of transition metal phosphides toward electrocatalytic water splitting: beyond noble metal catalysts

Cite this: *J. Mater. Chem. A*, 2024, 12, 28574

Basics, developments, and strategies of transition metal phosphides toward electrocatalytic water splitting: beyond noble metal catalysts

Yeongbin Lee,[†] Wooseok Jeong,[†] Yun Jae Hwang, Boeun An, Hyeonseok Lee, Heesoo Jeong, Gyuhyeon Kim, Yoonsu Park, Minyoung Kim and Don-Hyung Ha ^{*}

Electrocatalysts used for water electrolysis have been widely studied to decrease the overpotential and increase their stability and economic feasibility. Among the various candidates, transition metal phosphides (TMPs) display notably high electrocatalytic activity and stability under both acidic and alkaline conditions owing to the incorporation of P. As the number of studies focusing on TMPs has rapidly increased owing to their remarkable physicochemical properties, it is necessary to investigate the most recent advances in TMPs for hydrogen and oxygen evolution reactions (HER and OER, respectively). In addition to recent progress, this article arranges and reviews the HER and OER mechanisms, activity origins, synthetic processes that use various P sources, and effective strategies for enhancing the catalytic performance of TMPs. Furthermore, the current challenges faced by TMPs are discussed, indicating the route to be undertaken. Through this review article, we aim to guide future perspectives on TMP-based electrocatalysts for HER and OER.

Received 27th June 2024
Accepted 24th September 2024

DOI: 10.1039/d4ta04455j

rsc.li/materials-a

1. Introduction

The worldwide energy crisis demands the use of renewable energy sources instead of fossil fuels to reduce carbon compound emission-induced greenhouse effects.^{1,2} As an energy conversion strategy for storing and generating electricity from renewable energy sources, H₂ is actively used as an efficient gaseous energy carrier because of its high energy density.³ Numerous hydrogen production processes have been developed because of the importance of H₂ in the field of energy. Green hydrogen production *via* water electrolysis is the most promising method because it does not emit carbon or other pollutants.^{4,5} Water electrolysis involves two electrodes, a cathode for the hydrogen evolution reaction (HER) and an anode for the oxygen evolution reaction (OER). Both the HER and OER require a larger potential (overpotential) than that of the theoretical value. To minimize this overpotential, platinum group metals (PGMs) such as Ru, Rh, Pd, Os, Ir, and Pt have been commercially used as catalysts for the HER and OER.^{6–8} However, PGMs, which are rare, are expensive, thus, low-cost earth-abundant materials, such as transition metal-based catalysts are required.^{9,10}

Transition metal-based alloys, oxides, sulfides, carbides, nitrides, and phosphides have been used to synthesize inexpensive and highly active catalysts for the HER and OER.^{11–16}

Among these candidates, transition metal phosphides (TMPs) have attracted attention for use in water electrolysis because of their exceptional electrochemical performance.^{17,18} For example, the incorporation of P atoms can modulate the electronic structure, thereby enhancing electrocatalytic activity. The P atoms in the TMP structure can also provide high electrical conductivity, enabling control of the efficacy of HER and OER. In TMPs, the strong covalent bonds between the metal and P atoms ensure excellent mechanical robustness, facilitating long-term stability in both acidic and alkaline media. Additionally, TMPs are promising materials for use as HER and OER catalysts because of their high cost-efficiency and low toxicity.

The diverse advantages of using TMPs as electrocatalysts indicate that TMPs are one of the most challenging and rapidly evolving issues in water electrolysis. Many studies have been performed regarding the use of TMPs in water electrolysis, and their electrochemical performances have steadily improved as both HER and OER catalysts. Thus, the most recent progress, including the fundamentals governing both processes, should be professionally arranged and reviewed.

In this review article, we collate the available information regarding using TMPs for water electrolysis; the information begins with the fundamentals and builds toward the applications that comprise the HER and OER. Providing fundamentals of water electrolysis and TMPs can enable the beginners to be trained to prepare their future work. Moreover, we describe various methods for synthesizing TMPs using diverse P sources, thereby affording a selection of synthetic procedures that may be suited to specific experimental conditions. Additionally, by

School of Integrative Engineering, Chung-Ang University, 84 Heukseok-ro, Dongjak-gu, Seoul, 06974, Republic of Korea. E-mail: dhha@cau.ac.kr

[†] Yeongbin Lee and Wooseok Jeong equally contributed to this work.

introducing representative strategies to boost electrocatalytic activity, we aim to contribute to the future work of researchers and practitioners by providing in-depth insight into TMPs.

2. Fundamentals and evaluation of HER and OER

2.1. HER mechanism

During water electrolysis, HER occurs on the electrocatalyst surface of the cathode *via* complex reaction pathways (Fig. 1a). The reaction pathways for the HER comprise the Volmer–Heyrovsky and Volmer–Tafel steps regardless of the pH. In an acidic medium (normally H_2SO_4 aqueous solution), the Volmer step involves the adsorption of protons by reaction with electrons on the active sites of the HER catalysts, forming adsorbed hydrogen (H^*). Subsequently, the Heyrovsky or Tafel steps involve the evolution and release of H_2 molecules from the catalyst surface, depending on the H^* coverage. When the H^* coverage is low, H^* reacts with the proton in solution, including an electron (Heyrovsky step); and when the coverage is high two H^* molecules bond with each other, producing H_2 molecules (Tafel step).

Under alkaline conditions, (normally KOH aqueous solution), the Volmer–Heyrovsky and/or Volmer–Tafel mechanisms occur, albeit with different intermediates compared with those which form during acidic HER. Unlike in the acidic HER, the protons in the alkaline HER are supplied by H_2O molecules *via*

dissolution. Water dissociation leaves H^* on the catalyst surface and hydroxyl anions in solution. The Tafel reaction that occurs in an alkaline medium is identical to that of the acidic HER as the two H^* combine; by contrast, the Heyrovsky step involves the reaction between H^* and H_2O molecules. Owing to the limited proton concentration in alkaline media, the detailed reaction pathways that occur under alkaline conditions are more complex than those in acidic HER.

2.2. OER mechanism

In contrast to the HER, which requires two electrons, the OER requires four electrons to generate oxygen molecules at the anode, indicating that the OER has thermodynamically slower kinetics than those of the HER. Accordingly, the detailed OER mechanisms are more complicated than those of the HER. OER pathways are generally divided into two mechanisms: the adsorbate evolution mechanism (AEM) and the lattice oxygen (O^{2-}) mechanism (LOM). For AEM, hydroxyl anions (or H_2O molecules) are first adsorbed on M (active site, *) to form $^*\text{OH}$ species in alkaline (or acidic) media (Fig. 1b). The subsequent reaction with another OH^- , or electron removal, generates the $^*\text{O}$ from $^*\text{OH}$ depending on the pH of electrolyte. Further reactions induce oxyhydroxide ($^*\text{OOH}$), which releases the O_2 molecule *via* single-electron transfer, following the AEM pathways. The initial two steps of the LOM, that is, adsorption on M to the generation of $^*\text{O}$ are identical to those of the AEM, whereas the subsequent steps differ from those of the AEM

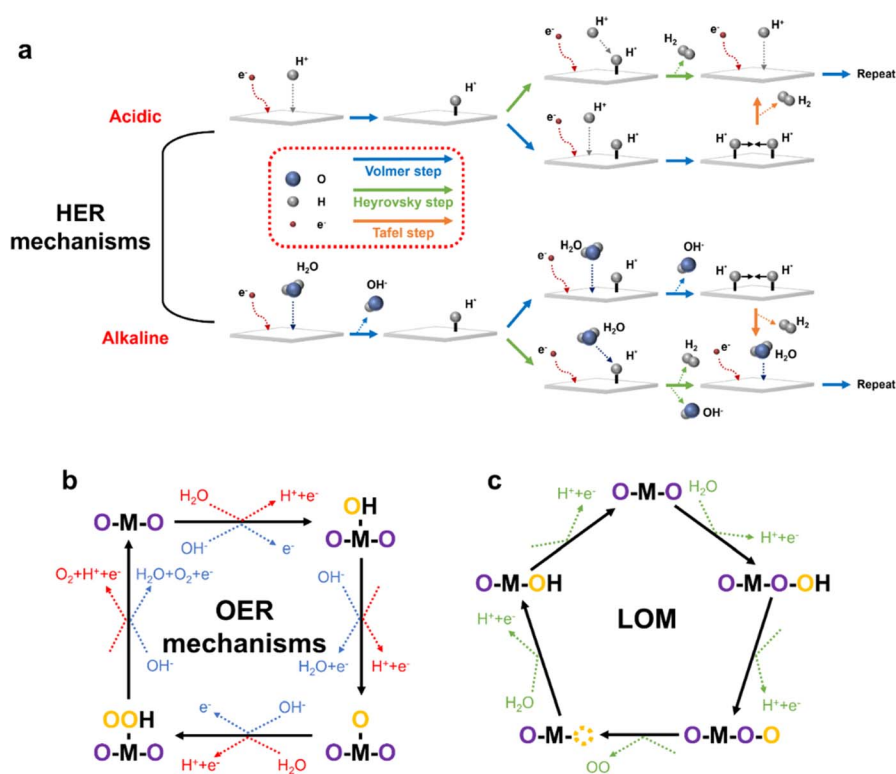


Fig. 1 (a) Schematic illustration of hydrogen evolution reaction mechanisms in both acidic and alkaline media. Diagrams of oxygen evolution reaction mechanisms of (b) adsorbate evolution mechanism (AEM) (red and blue lines for acid and alkaline conditions, respectively) and (c) lattice oxygen mechanism (LOM).

processes. During LOM, *O reacts with lattice oxygen, resulting in O_2 release by forming oxygen vacancies (Fig. 1c). These oxygen vacancies can be refilled by hydroxyl anions or water molecules that migrate from the solution. The refreshed M sites are obtained after the release of H from the catalyst surface.

2.3. Overpotential and identification of intrinsic property

Theoretically, a potential of ~ 1.23 V between the cathode and anode is required for water electrolysis because the standard electrode potentials of the HER and OER are 0 and 1.23 V under standard conditions, respectively (Fig. 2). However, practical water electrolysis requires a potential higher than the theoretical value of 1.23 V. The additional potential from 1.23 V is an overpotential (η) for overall water splitting, which is the sum of the overpotentials of HER (η_{HER}) and OER (η_{OER}). Overpotential is a major descriptor used to evaluate the electrochemical catalytic performance of cathodes and anodes. An efficient catalyst requires the overpotential to be as low as possible to reduce energy consumption. The overpotential is usually evaluated using polarization curves that show the correlation between the current density and overpotential (Fig. 2).

The electrocatalysts with outstanding performance usually show impressive intrinsic properties for water splitting. The intrinsic activity of HER and OER catalysts can be investigated through polarization curve normalized by electrochemical surface area (ECSA) value demonstrating the total area of HER and OER active sites. Accordingly, ECSA-normalized polarization curve is a tool to confirm the intrinsic activity of synthesized electrocatalysts. The turnover frequency (TOF) is another representative factor for elucidating the intrinsic activity of catalyst materials. The TOF value is the number of conversions at an active site per unit time, which indicates the electrocatalytic activity for the HER and/or OER. The TOF, as a function of the overpotential, is calculated using eqn (1).

$$\text{TOF} = \frac{J \times N_A}{n \times F \times \tau}, \quad (1)$$

where J is the current density at a specific overpotential, N_A is Avogadro's number, n is the number of electrons, F is Faraday's constant, and τ is the number of electrochemical active sites.²⁰ Additionally, rotating ring-disk electrode (RRDE) analysis is another method to define the actual OER active sites as well as to explore evolution of structure reconstruction of the TMP catalyst.^{21,22} The O_2 gas evolved on disk electrode is transported to the ring electrode through convection, permitting the reduction of O_2 to H_2O at ring electrode. As ring current depends on O_2 concentration, the alkaline OER onset potential is decided by the ring current. The RRDE also allows the calculation of faradaic efficiency using ring and disk currents, meaning that RRDE is powerful technique to figure out the real OER active site and to evaluate the intrinsic property and efficiency of catalyst materials.²³

2.4. Tafel slope and exchange current density

The Tafel slope represents a linear correlation between the overpotential and current density, which can be obtained by replotting the polarization curve on a logarithmic scale. Electrocatalytic performance is estimated from the Tafel slopes. Because the Tafel slope indicates the kinetic barrier, a lower value implies faster catalytic kinetics. In addition, the Tafel slope is used to determine the rate-determining step (RDS) of the HER based on its value in the Volmer, Tafel, and Heyrovsky steps. An additional descriptor, the exchange current density, is the value of the current density when the anodic current reaches the cathodic value (dynamic equilibrium). This parameter is determined mainly by the catalyst material, temperature, and solution conditions. In addition, the exchange current density is proportional to the intrinsic activity of the catalyst material, as it represents the electron transfer and electrode reaction capabilities. In other words, an electrode with a catalyst and

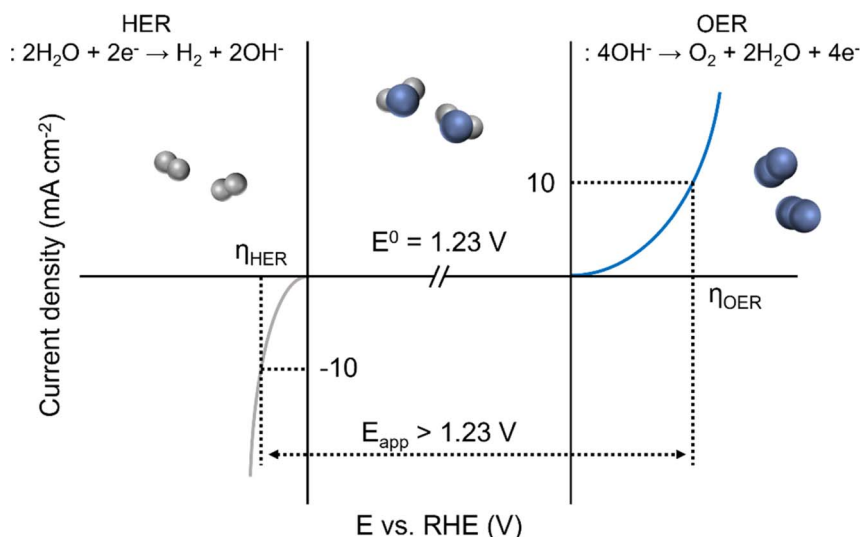


Fig. 2 Typical polarization curves of hydrogen evolution reaction (HER) (left, gray) and oxygen evolution reaction (OER) (right, blue). Adapted with permission.¹⁹ 2017, John Wiley and Sons.

large exchange current density requires a low current driving force. For example, Pt catalysts, among some of the best commercial catalysts, display an ultra-large exchange current density of $\sim 1 \times 10^{-3} \text{ A cm}^{-2}$, while Hg catalysts exhibit poor HER activity and record an exchange current density of $\sim 5 \times 10^{-13} \text{ A cm}^{-2}$ in 0.5 M H_2SO_4 solution.^{24,25}

2.5. Stability

Catalytic stability as well as the overpotential is highly important parameter for evaluating electrocatalysts, because of their reliability in practical water electrolysis. Stability tests can be conducted using various techniques such as chronopotentiometry/chronoamperometry, repeated cyclic voltammetry (CV), and linear sweep voltammetry (LSV). Chronopotentiometry (CP) and chronoamperometry (CA) tests measure the change in potential and current density at various time scales, from minutes to days, when a consistent current and potential are applied. The highly stable catalysts maintain their electrocatalytic performances for longer durations. The latter CV and/or LSV measurements are usually performed by confirming the decrease in overpotential from repeated CV and/or LSV curves. Dozens and thousands of cycles enabled the observation of real-time degradation of catalytic performance. For quantitative analysis, the stability of a sample is commonly evaluated at a specific current density, such as 10 mA cm^{-2} .

The catalyst stability is determined by diverse factors in both chemical and physical aspects. In a chemical point of view, the catalyst materials undergo degradation through electrolyte effect and repeated redox reactions under applied potential, which can induce the metal element leaching. Subsequently, the metal cations leached out redeposited on the catalyst surface, causing rapid decrease in catalyst performance. The composition control and/or replacement to other element can prevent the dissolution of metal species during electrochemical reactions by modifying the surface nature of catalyst materials. The representative physical reasons to lowering stability are adhesion of electrode components, crack issue, and catalyst morphology. The catalysts can be detached from the electrode to bulk solution when the adhesions between materials themselves or catalyst and substrate are not enough to overcome the harsh conditions come from electrode potential, pH, and temperature, which diminishes the sustainability of electrode. In these conditions, catalyst crack or delamination can be also formed by corrosion and other mechanical stresses, which can further accelerate the catalyst degradation. To minimize the formation of crack or delamination, use of specific binder, electrode patterning, and film thickness control can be adopted by mitigating the mechanical and electrochemical stresses.²⁶ Additionally, catalyst materials showing high resistance to heat, tensile strength and compression should be selected to reduce the mechanical degradation of electrode, and advance of coating process is also required to provide strong adhesion between catalyst and substrate.^{27,28} The fine construction of catalyst morphology is highly critical to easily release the gas bubbles that can prohibit the active sites as well as to maximize the exposure of active sites. Accordingly, many studies have

developed and optimized the morphology of phosphide catalyst to reduce the adhesive force between electrodes and bubbles and to obtain reliable performance stability.^{29,30} Additional to the catalyst morphology, the catalyst wettability is highly significant to obtain high performance catalyst, for example, an ideal catalyst has to be hydrophilic and aerophobic, enabling the exposure of active sites to electrolyte and fast release of bubble products.³¹

2.6. Faradaic efficiency

The faradaic efficiency (FE) is defined as the efficiency of charge transfer in generating the targeted reaction. FE is normally calculated from the H_2 yield by considering both the ideal and actual H_2 gas quantities. Gas chromatography or water-gas displacement can be used during chronopotentiometry or chronoamperometry to experimentally obtain the actual amount of the product. By contrast, the theoretical H_2 production can be assumed using a constant current or potential.

3. Activity origins and characteristics of TMPs

3.1. Critical role of P

TMPs are alloys composed of transition metals and P atoms that form crystal lattices. Because P atoms normally have a higher electronegativity than those of transition metals (M), M(metal)-P bonds within TMPs act as a bridge to deliver electrons from the metals to the anionic P sites. The coordination change from M-M to M-P leads to different configurations of the elements, implying modifications in the electronic structures and catalytic performance. Such coordination changes can be easily accomplished by controlling the ratio of M to P in the crystal structure of TMPs. For example, Ha *et al.* colloiddally synthesized mono-metallic hollow cobalt phosphide nanoparticles with different P/Co ratios, and discovered that higher P incorporation resulted in higher HER activity (Fig. 3a).³² Cho *et al.* synthesized three types of colloidal nanoparticles (Fe, Fe_2P , and FeP), as depicted in the transmission electron microscopy (TEM) images in Fig. 3b. When these nanoparticles of Fe, Fe_2P , and FeP were used as HER catalysts, the FeP sample, which had the highest P/Fe ratio exhibited the best HER activity compared with those of the other catalysts (Fig. 3c).³³ Among the nickel phosphides, the Ni_5P_4 sample displayed the best HER performance than those of the other samples that comprised different stoichiometries, namely, Ni_{12}P_5 and Ni_2P .³⁵ This dependence of the HER activity on the P ratio was also confirmed for molybdenum phosphides (Fig. 3d).³⁴

Additionally, the P concentration in the TMP lattice is proportional to the stability of the sample in an acidic environment because metal dissolution is thermodynamically suppressed. The reliable and excellent stability is due to the M-P bond (strong covalent bond), which ensures good mechanical hardness and excellent electrochemical resistivity. In particular, metal-rich phosphides, such as Mo_3P and Ni_3P , can exhibit the exceptional conductivity of pure metals or even superconductors.³⁶ However, too many P atoms can decrease the electronic

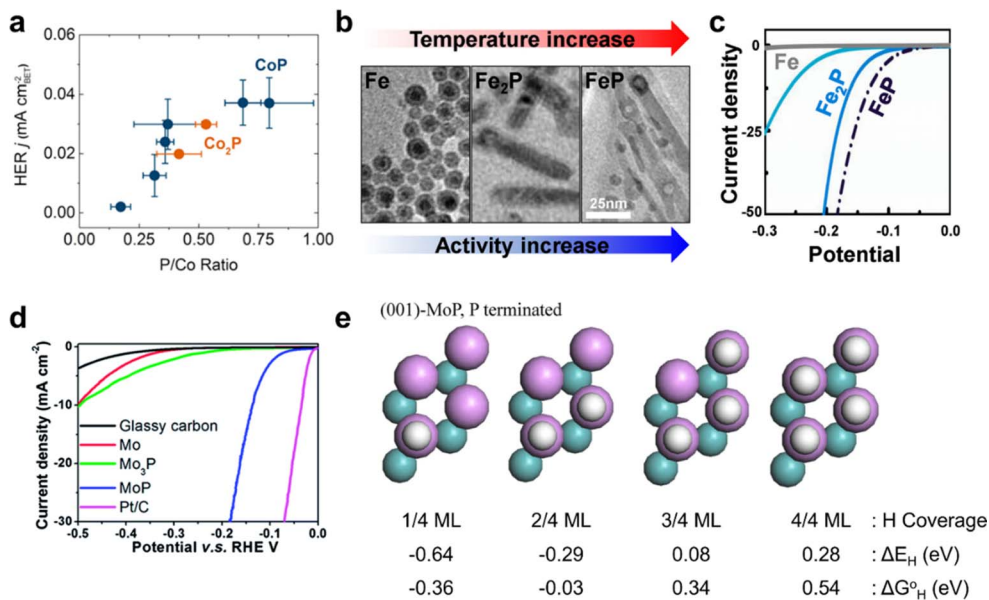


Fig. 3 (a) Current densities of hydrogen evolution reaction as a function of P/Co ratio for cobalt phosphide nanoparticles in alkali solution, showing higher HER activity in higher P concentration. Reprinted with permission.³² 2016, Elsevier. (b) Transmission electron microscopy images and (c) LSV curves of the iron phosphide nanoparticles depending on their phase transformations. Reprinted with permission.³³ 2018, Elsevier. (d) LSV curves of Mo, Mo₃P, and MoP in acidic condition of 0.5 M H₂SO₄. (e) Hydrogen adsorbed (001) facet of MoP, which was terminated by P atoms. (d and e) Reprinted with permission.³⁴ 2014, Royal Society of Chemistry.

conductivity of TMPs to that close to those of semi-conductors or insulators.^{24,37} To optimize the HER performance of TMPs, a balanced atomic ratio between the transition metal and P atoms must be accomplished.

3.2. OER-induced surface reconstruction of TMPs

The surface reconstruction effects of TMPs during OER have been widely studied. The surface P atoms ensure the metal atoms are positively charged, enabling binding to oxide species.³⁸ Accordingly, oxides and/or (oxy)hydroxides form on the surface of TMPs during OER owing to thermodynamic instability inducing oxidation in the anodic potential region in alkaline electrolytes.^{38–41} The phosphide-oxide interface on the surface can improve charge transfer toward active sites.¹⁴ These oxidized phases, which are the actual active sites for the OER, alter the surface configuration of the TMPs by lowering the crystallinity by incorporating various types of defects,^{42,43} thereby protecting the phosphide core from further corrosion. Those studies have revealed that understanding the catalyst surface change during OER is highly significant as it can provide insight to modifying the catalyst activity and stability. Such surface reconstructions through the formation of oxides and (oxy)hydroxides are mainly identified by adopting *in situ* Raman spectroscopy and other *ex situ* analyses such as X-ray photoelectron spectroscopy (XPS) and X-ray absorption spectroscopy (XAS). *In situ* Raman analysis provides information of surface adsorbates such as (oxy)hydroxides, while XPS and XAS inform the oxidation state change of the components after OER. However, it is challenging to understand the exact surface change and reconstruction process when the catalyst of

complex composition, such as high-entropy materials, is utilized.⁴¹

3.3. Electronic structure

Although ideal electrocatalysts require a high intrinsic activity, they are mainly limited to the PGMs.⁴⁴ To mitigate this problem, modulation of the electronic structure of transition metals, including TMPs, has been actively studied. The introduction of P atoms into transition metal lattices leads to a change in the d-band center and Fermi level of the transition metal center. TMPs with modified electronic structures are acknowledged as being highly efficient catalysts for the HER and OER because their electronic structures are similar to those of Pt.⁴⁵

The electronic structures of the TMPs were investigated by density functional theory (DFT). The change in electronic structures that occurs when P atoms form bonds with Ni metal has been revealed by the total density of states (DOS) of samples calculated using DFT.⁴⁶ Ni₂P may have the best catalytic activity for hydrodesulfurization and hydrodenitrification compared with those of Ni₃P, Ni₁₂P₅, and Ni₅P₄. Additionally, the electronic effect on the catalytic potential when N, C, and P atoms form structures with Mo atoms has been investigated. DFT calculations have shown that MoP displays the most efficient catalytic activity for CO and S adsorption compared with those of Mo, MoN, and MoC, thereby demonstrating the superiority of phosphides as catalysts.⁴⁷ These excellent properties of phosphides are due to the transfer of a small number of electrons from the Mo to P atoms, and the subsequent negligible downward shift in the Mo 4d states. Briefly, the introduction of P changes the electronic structures of the transition metals by

constructing TMPs, indicating the significant effect of P on catalysis.

3.4. Gibbs free energy of hydrogen adsorption

A representative descriptor, the Gibbs free energy for hydrogen adsorption (ΔG_{H^*}), evaluates the intrinsic activity of the catalyst for acidic HER. A negative value of ΔG_{H^*} indicates strong binding of protons on the catalyst surface, whereas a positive ΔG_{H^*} prevents the attachment of protons, thereby reducing the catalytic performance. This phenomenon is well known as the Sabatier principle. The Sabatier principle states that a moderate ΔG_{H^*} (near zero) for intermediate adsorption is required to exhibit optimized HER performance.⁴⁸ TMPs follow the Sabatier principle, and display a volcano trend dependent on their elements and compositions.

The higher electronegativity of P atoms compared with those of transition metals enables the anionic P sites to easily accept protons at low hydrogen coverage on the TMP surface.¹⁴ By contrast, hydrogen atoms can be detached at anionic P sites on the surface at high hydrogen coverage, thereby indicating the presence of optimal and abundant active sites for the HER. For example, the P-terminated (001) facet of MoP easily accepts hydrogens at P atoms under low hydrogen coverage when ΔG_{H^*} is negative while the hydrogens displayed a tendency to be removed from the P site at high coverage when ΔG_{H^*} is positive value (Fig. 3e).³⁴ Aside from MoP, various TMPs exhibit excellent intrinsic activities for HER as the ΔG_{H^*} value changes from negative to positive when the hydrogen coverage increases.⁴⁹ These results indicate that P atoms have a positive effect on hydrogen production.

4. Synthesis of TMPs

4.1. Phosphorous sources for TMPs synthesis

4.1.1. Organophosphorus sources. Organophosphorus sources (TOP, TPP, and TOPO) are widely used as phosphorus sources for the solution-phase synthesis of TMPs. In this approach, the C–P bonds of the organophosphorus sources undergo cleavage at an elevated temperature (*ca.* 300 °C). Following thermal activation, the liberated P atoms react with metal species derived from various sources, including metal nanoparticles, metal acetylacetonates, and metal carbonyl compounds.

These reactions are conducted in a heated organic solvent, such as oleylamine, 1-octadecene, or squalene, under an inert atmosphere to prevent unwanted oxidation. Schaak's group successfully synthesized a range of transition metal-based phosphides (iron-, cobalt-, nickel-, tungsten-phosphide, *etc.*)^{50–54} and noble metal-based phosphides (rhodium, palladium-, platinum-, and gold-phosphide)⁵⁵ using TOP as the P source. Park *et al.* fabricated iron phosphide nanoparticles from various P sources (TOP, TPP, tris(diethylamino)phosphine (TEAP), and tri-*n*-butylphosphine (TBP)).⁵⁶

The solution-phase approach provides a versatile platform for the synthesis of TMPs with diverse compositions, allowing precise control over their size and morphology by the

adjustment of key synthetic parameters, such as the precursor combination, molar ratio of metal to phosphorus, temperature, and reaction time. For example, Pan *et al.* synthesized phase-controlled nickel phosphide nanocrystals (Ni_{12}P_5 , Ni_2P , and Ni_5P_4 NCs) by varying the P/Ni precursor ratio and demonstrated their phase-dependent HER activities.³⁵ Using TOPO as both a solvent and P source, Robinson's groups demonstrated the morphological evolution of hyperbranched Co_2P .⁵⁷ Nevertheless, it is important to note that organophosphorus sources present challenges related to toxicity and flammability.

4.1.2. Hypophosphite/ PH_3 gas. Hypophosphite compounds (NaH_2PO_2 and $\text{NH}_4\text{H}_2\text{PO}_2$) or PH_3 gas are typical phosphorus sources that are used in gas–solid reactions. Hypophosphite is often preferred due to the high toxicity of PH_3 gas. Upon decomposition at temperatures exceeding 250 °C ($\text{NaH}_2\text{PO}_2 \rightarrow \text{PH}_3(\text{g}) + \text{Na}_2\text{HPO}_4$), hypophosphite releases PH_3 gas, facilitating the synthesis of TMPs *via* reactions with various metal sources. These materials include metal oxides,⁵⁸ metal hydroxides,⁵⁹ metal supports,⁶⁰ and metal–organic frameworks (MOFs).⁶¹

Novel synthesis methods using PH_3 gas plasma have also been developed. Liang *et al.* demonstrated the plasma-enhanced synthesis of TMP using a chemical vapor deposition (PECVD) system, that produces NiCoP nanoplates which display exceptional catalytic performance for overall water splitting.⁶² Zhang *et al.* developed a plasma-assisted strategy, accomplishing the first-ever synthesis of TMP thin film *via* atomic layer deposition (ALD).⁶³ In addition, hypophosphite can be used as a phosphorus source in electrodeposition. For instance, Chen *et al.* used hypophosphite to produce an amorphous high-entropy CoFeNiCrMnP compound on Ni foam (NF) *via* one-step electrodeposition.⁶⁴ Notably, high-entropy electrocatalysts comprising transition metals have demonstrated higher activity than those of noble-metal catalysts. Although gas–solid reactions using hypophosphite/ PH_3 are useful for fabricating uniquely structured TMPs, this approach is not suited to achieving precise composition control.

4.1.3. Red phosphorus. Red phosphorus (RP) is an alternative source of P for gas–solid reactions and generates phosphorus vapor at elevated temperatures. This process involves placing the metal source and RP in a tube furnace, with the RP positioned closer to the upstream side. TMPs are synthesized *via* a reaction between the metal source and RP upon heating in an inert atmosphere.

Yao *et al.* synthesized self-supported $\text{Cu}_3\text{P}/\text{CF}$ by phosphorizing copper foam (CF) with RP.⁶⁵ Similarly, Pu *et al.* formed a WP nanorod array on a carbon cloth (WP NAs/CC) by reacting a WO_3/CC precursor with RP.⁶⁶ Direct phosphorization using RP is particularly favored for fabricating P-rich TMPs, as exemplified by Jiang *et al.*, who synthesized FeP_2/C nanohybrids using one-step phosphorization.⁶⁷ Furthermore, Fransær's group successfully synthesized CoP_3 nanocages by annealing a Co_3O_4 precursor with RP; a high alkaline OER performance was noted.⁶⁸

Alternatively, a series of TMPs (Fe_2P , Co_2P , Ni_2P , Cu_3P , *etc.*) can be obtained *via* solvothermal^{69,70}/hydrothermal processes,^{71,72} in which metal precursors react with RP at

relatively low temperatures (*ca.* 200 °C). Although these strategies are known for their operational simplicity and environmental friendliness, they often require prolonged reaction times.

4.1.4. Phosphate/phosphorus acid. Phosphates ($\text{NH}_4\text{H}_2\text{PO}_4$ and $(\text{NH}_4)_2\text{HPO}_4$) are commonly used as P sources in the temperature-programmed reduction (TPR) method.^{73–76} In this technique, TMPs are fabricated *via* the reduction of metal phosphates at high temperatures, typically approximately 650 °C, under a H_2 atmosphere. This procedure involves the evaporation and calcination of a solution containing a metal salt and phosphate in water. The resulting powder is then reduced with H_2 to synthesize TMPs.

For example, Sun's group used this method to prepare WP_2 submicroparticles (WP_2 SMPs) *via* the direct reduction of metal phosphates.⁷⁴ Phillips *et al.* synthesized MoP using the same method.⁷⁵ In 2020, Gao's group introduced a sol-gel process using $\text{NH}_4\text{H}_2\text{PO}_4$ as a P source to fabricate carbon-supported TMPs@C.⁷⁷ A series of TMPs from mono- to trimetallic phosphides were successfully synthesized *via* the carbonization of gel ash. The resulting NiFeP@C exhibited excellent performances as HER and OER catalysts in alkaline media.

In addition, an innovative synthetic approach based on TPR was proposed by Cecilia *et al.*,⁷⁸ who used phosphorus acid ($\text{H}_2\text{PO}_3\text{H}$) as the P source and nickel hydroxide as the Ni source, demonstrating the direct reduction of $\text{Ni}(\text{HPO}_3\text{H})_2$ salt to obtain Ni_2P at a relatively low temperature (375–425 °C). This novel methodology provides a promising avenue for the controlled synthesis of TMPs with enhanced efficiency.

4.1.5. Black phosphorus (or phosphorene)/yellow phosphorus. Black phosphorus (BP) is the most stable form of elemental phosphorus and is characterized by its nontoxicity and nonflammability. Xue *et al.* introduced a high-energy ball milling (HEBM) technique for the preparation of BP from RP and extended this method to synthesize Co_xP at room temperature.⁷⁹ The resulting Co_xP exhibits bifunctional electrocatalytic properties, surpassing those of conventional Pt/C|| RuO_2 catalysts in alkaline media.

Furthermore, BP can take the form of 2D nanosheets, which are commonly referred to as phosphorenes. For instance, Yan's group successfully exfoliated BP nanosheets from bulk BP crystals using sonication.⁸⁰ The researchers synthesized Ni_2P nanocrystals on the BP nanosheets, creating a unique 0D–2D heterostructure *via* a subsequent solvothermal process. The Ni_2P @BP composite, which displays enhanced electrical conductivity and reduced thermal conductivity compared with those of pure BP nanosheets, demonstrated exceptional performance as an electrocatalyst for the HER.

In addition to these advancements, Hou *et al.* fabricated Co_2P hollow spheres by reacting Co^{2+} ion with PH_3 , generated *via* the reaction of yellow P and ethanol at high temperature (220 °C) and pressure.⁸¹ Similarly, Gillan's group used yellow P as a P source in a low-temperature solvothermal method to produce phosphorus-rich TMPs, including CoP_3 , NiP_2 , and CuP_2 .⁸² These diverse approaches demonstrate the versatility of BP and its derivatives in the synthesis of advanced materials for catalytic applications.

4.1.6. Phytic acid. Phytic acid (PA), recognized for its environmentally friendly and nontoxic nature, contains six phosphate groups that can serve as P sources for producing TMPs *via* phosphate reduction using H_2 . In 2016, Li *et al.* pioneered the synthesis of TMPs derived from phytic acid,¹¹² and synthesized CoP and MoP *via* the pyrolysis of PA-chelated metal complexes in a reductive atmosphere. Wang *et al.* used PA as an etchant for ZIF-67 and as a P source.¹¹³ The PA etching process used to produce ZIF-67 formed a porous structure of Co-PA nanoboxes. Subsequently, under H_2 pyrolyzing conditions, hierarchical porous CoP/C nanoboxes were successfully synthesized. When used as an electrocatalyst for HER, this material exhibited excellent electrocatalytic performance. Moreover, Ramos-Fernandez's group introduced a novel microwave-assisted approach that proved to be a more facile and faster strategy than that of traditional pyrolysis methods.¹¹⁴

4.1.7. Other phosphorus sources. In addition to the aforementioned common P sources, various alternative sources can be used to synthesize TMPs. Li *et al.* synthesized CuP_2 @C for lithium-ion batteries by reducing PCl_3 in a molten salt at low temperatures.¹¹⁵ Furthermore, Schipper *et al.* prepared phase-pure iron phosphide thin films (FeP , Fe_2P , and Fe_3P) using the metal-organic chemical vapor deposition from single-source precursors (SS-MOCVD), thereby demonstrating a phase-dependent trend in HER activity.¹¹⁶

Zhao *et al.* used HDTMPA with a high P content unprecedentedly as the P source, successfully synthesizing a range of TMP/NC heterostructures (RhP_2 @NC, FeP @NC, CoP @NC, Ni_2P @NC, and Cu_3P @NC).¹¹⁷ Moreover, large scale TMP-based electrodes can be synthesized *via* a simple inkjet printing process using metal compound solution and ionic liquid ([BMIM]· PF_6).¹¹⁸

Additionally, phosphorus-containing polymers, such as glyphosine, serve as effective sources, for TMPs synthesis *via* pyrolysis.¹²⁰ Biomass, exemplified by *Saccharomyces*/yeasts, is an economical, ecofriendly, and green P source. For example, Li *et al.* used *Saccharomyces* as both a carbon template and P source to produce TMPs.¹²¹ Similarly, Wan *et al.* demonstrated the utility of yeast, with its high P content, as a versatile platform for synthesizing various metal phosphides (Co_2P , Mn_2P , Zn_3P_2 , and Ni_2P).¹²²

As discussed in this section, diverse methods and sources of P can be used to synthesize different types of TMPs. For example, thermal decomposition methods are commonly used TOP as P source, whereas hypophosphites are used in several synthetic approaches. The TMPs synthesized using various combinations of methods and P sources exhibited excellent catalytic behavior for water electrolysis under both acidic and alkaline conditions. The details of the catalyst preparation and water electrolysis performance are summarized in Table 1.

4.2. Characteristics of synthesis methods

The synthetic approaches for preparing TMPs can be broadly categorized into solid- and liquid-phase synthesis methods, each utilizing suitable phosphorus sources (Fig. 4). Table 2 below outlines the advantages and disadvantages of these

Table 1 Summary of the water electrolysis performances of TMPs-based electrocatalysts^a

Materials (P source)	Substrate	HER/OER/overall	Performance	Electrolytes	Reference
FeP (TOP)	CP	HER	38 mV@10 mA cm ⁻²	0.5 M H ₂ SO ₄	9
MoP (TOP)	Ti foil	HER	177 mV@10 mA cm ⁻²	0.5 M H ₂ SO ₄	83
WP (TOP)	Ti foil	HER	120 mV@10 mA cm ⁻²	0.5 M H ₂ SO ₄	54
Cu ₃ P (red P)	Cu mesh	HER	117 mV@10 mA cm ⁻²	0.5 M H ₂ SO ₄	84
Ce-Ni ₂ P (NaH ₂ PO ₂)	Ti mesh	HER	42 mV@10 mA cm ⁻²	0.5 M H ₂ SO ₄	85
Co-MoP (TOP)	Ti foil	HER	167 mV@10 mA cm ⁻²	0.5 M H ₂ SO ₄	86
Ni ₂ P/Ni ₅ P ₄ (NaH ₂ PO ₂)	GCE	HER	78 mV@10 mA cm ⁻²	0.5 M H ₂ SO ₄	59
NiP ₂ /Ni ₅ P ₄ (red P)	NF	HER	249 mV@2 A cm ⁻²	0.5 M H ₂ SO ₄	87
Fe _{0.5} Ni _{1.5} P (TOP)	GCE	HER	163 mV@50 mA cm ⁻²	0.5 M H ₂ SO ₄	88
V-CoP/Ni ₂ P (NaH ₂ PO ₄)	NF	HER	79 mV@10 mA cm ⁻²	0.5 M H ₂ SO ₄	89
B-CoP (NaH ₂ PO ₂)	Ti mesh	HER	112 mV@100 mA cm ⁻²	1 M KOH	90
Cr-CoP (NaH ₂ PO ₂)	CC	HER	36 mV@10 mA cm ⁻²	1 M KOH	91
MoP ₂ -NiCoP (NaH ₂ PO ₂)	NF	HER	50 mV@10 mA cm ⁻²	1 M KOH	92
ZnO-Ni ₂ P (NaH ₂ PO ₂)	NF	HER	68 mV@10 mA cm ⁻²	1 M KOH	93
B,V-Ni ₂ P (NaH ₂ PO ₂)	NF	HER	148 mV@100 mA cm ⁻²	1 M KOH	94
FN-CoP (NaH ₂ PO ₂)	CC	HER	66 mV@10 mA cm ⁻²	1 M KOH	95
Cu ₁ Co ₂ -Ni ₂ P (NaH ₂ PO ₂)	NF	HER	51 mV@10 mA cm ⁻²	1 M KOH	96
Mo-Ni ₂ P _x @MNF (NaH ₂ PO ₂)	MNF	HER	62 mV@100 mA cm ⁻²	1 M KOH	60
Ni-Co-Fe-P (NaH ₂ PO ₂)	NF	HER	64 mV@10 mA cm ⁻²	1 M KOH	97
CoFeNiCrMnP (Na ₂ HPO ₂)	NF	HER	51 mV@100 mA cm ⁻²	1 M KOH	64
CoP ₃ (red P)	CFP	OER	334 mV@10 mA cm ⁻²	1 M KOH	98
Fe-Ni ₂ P (NaH ₂ PO ₂)	NiFe foam	OER	218 mV@100 mA cm ⁻²	1 M KOH	99
Sn-Ni ₅ P ₄ (red P)	CF	OER	173 mV@10 mA cm ⁻²	1 M KOH	100
F-CD/CoP (NaH ₂ PO ₂)	NF	OER	161 mV@20 mA cm ⁻²	1 M KOH	101
CoNiP _x @FeCoP _x /C@CoNiP _x (NaH ₂ PO ₂)	NF	OER	298 mV@10 mA cm ⁻²	1 M KOH	61
Ni ₅ P ₄ @NiOOH (NaH ₂ PO ₂)	CC	OER	273 mV@50 mA cm ⁻²	1 M KOH	102
Ni ₅ P ₄ @FeP (NaH ₂ PO ₂)	NF	OER	242 mV@100 mA cm ⁻²	1 M KOH	103
Ni-Mn-FeP (NaH ₂ PO ₂)	NiFe foam	OER	185 mV@10 mA cm ⁻²	1 M KOH	104
S-NiFeP (NaH ₂ PO ₂)	CC	OER	201 mV@10 mA cm ⁻²	1 M KOH	105
CNT-Co _{1.33} Fe _{0.67} P _x (TBP)	NF	OER	299 mV@100 mA cm ⁻²	1 M KOH	106
NiCoP (NaH ₂ PO ₂)	NF	Overall	1.981 V@1 A cm ⁻²	1 M KOH	107
Ni _{0.97} Co _{0.04} P (red P)	NF	Overall	1.71 V@500 mA cm ⁻²	1 M KOH	108
Fe _{0.5} CoNi _{0.5} P (TOP)	NF	Overall	1.52 V@10 mA cm ⁻²	1 M KOH	109
Ni-Co-Fe-P nanobricks (NaH ₂ PO ₂)	NF	Overall	1.46 V@10 mA cm ⁻²	1 M KOH	110
NiFeP (phosphorus powder)	NiFe foam	Overall	1.57 V@100 mA cm ⁻²	Alkaline simulated seawater	111

^a GCE: glassy carbon electrode, MNF: molybdenum-nickel foam, NF: nickel foam, CF: carbon fiber, CFP: carbon fiber paper, CP: carbon paper, CC: carbon cloth.

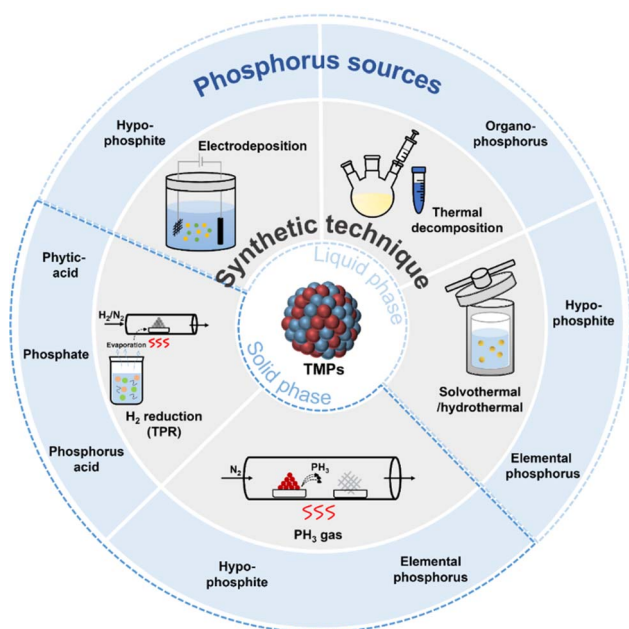


Fig. 4 Schematic illustration of representative synthetic techniques and phosphorus sources for TMPs.

synthesis methods, offering guidance for selecting the most appropriate approaches based on experimental conditions. Additionally, beyond the methods listed in Table 2, microwave-assisted,¹¹⁴ and plasma-enhanced^{62,63} synthetic strategies, among others^{77,79,118} have also proven to be effective for synthesizing TMPs. Through these techniques, TMPs can be designed with unique morphology, composition, even when using identical materials, to optimize their specific properties that enhance their catalytic performance. However, it is important to note that the comparing the electrochemical properties of identical-phase TMPs synthesized *via* different methods is relatively complicated, as potential variables, particularly size and shape, can influence catalytic performance. For example, nickel phosphides, prepared by an annealing method¹²³ and a thermal decomposition method,¹²⁴ respectively, despite both being in the Ni₂P phase, exhibited quite different OER activity. In the study by Wang *et al.*, however, the Ni₂P synthesized *via* the annealing method showed similar performance to that of the thermal decomposition method.¹²⁵ Such variations likely originated from

Table 2 Summary of advantage and disadvantage of TMPs synthetic methods

Synthetic method	Phosphorus source	Advantage	Disadvantage	
Solid phase	Annealing (PH ₃ gas)	Hypophosphite, elemental phosphorus	Facile, prepare unique morphology	Generate toxic PH ₃ gas
	H ₂ reduction (TPR)	Pytic acid, phosphate, phosphorus acid	Economical, green and nontoxicity	High reaction temperature
Liquid phase	Thermal decomposition	Organophosphorus	Precise control of size and morphology	Toxicity, flammability
	Solvothermal/hydrothermal	Hypophosphite/elemental phosphorus	Low reaction temperature	Prolonged reaction time, high pressure
	Electrodeposition	Hypophosphite	One-step process, easily prepare multicomponent materials	Difficult to set-up, limited substance

differences in morphological characteristics and crystallinity rather than the synthesis method itself.

5. Performance enhancement strategies

5.1. Composition–performance relationship

The electrochemical properties of TMPs can be precisely tuned by manipulating their metal-to-phosphorus stoichiometry. For instance, nickel phosphides (Ni_xP_y) can occur in at least seven distinct Ni/P ratios (Ni₃P, Ni₁₂P₅, Ni₂P, Ni₅P₄, NiP, NiP₂, and NiP₃), each of which influences the HER catalytic activity owing to changes in their electronic structures.¹²⁶ In 2023, Rappe *et al.* conducted atomistic computational calculations to investigate the correlation between the surface reconstruction of various Ni_xP_y compositions and their HER activities in an electrochemical environment.¹¹⁹ Under these reaction conditions,

surface reconstruction occurred with H coverage, and the formation of phosphorus vacancies (P_v) significantly influencing the catalytic properties (Fig. 5a). Under acidic conditions, Ni₃P and Ni₅P₄ were predicted to require the lowest overpotential, followed by Ni₂P and Ni₁₂P₅. Interestingly, this trend aligned well with that of the experimental results reported by Liu *et al.*³⁵ The formation of P_v reduced the catalytic activity toward the HER. The DFT calculation results clarified the nature of H binding and provided insight into the optimal design of active sites to enhance catalytic performance. Another study presented the Ni–P bond length as a descriptor to compare the origin of the enhanced HER activity in Ni₅P₄ compared to Ni₂P.¹²⁷ Both Ni₅P₄ and Ni₂P share an identical Ni₃ hollow site, which serves as the adsorption site for H. The study revealed that Ni₅P₄ exhibited an increased Ni–P bond length relative to Ni₂P, correlating with its superior HER performance. This observation suggests that the elongation of the Ni–P bond in Ni₅P₄ plays a crucial role in enhancing its catalytic activity.

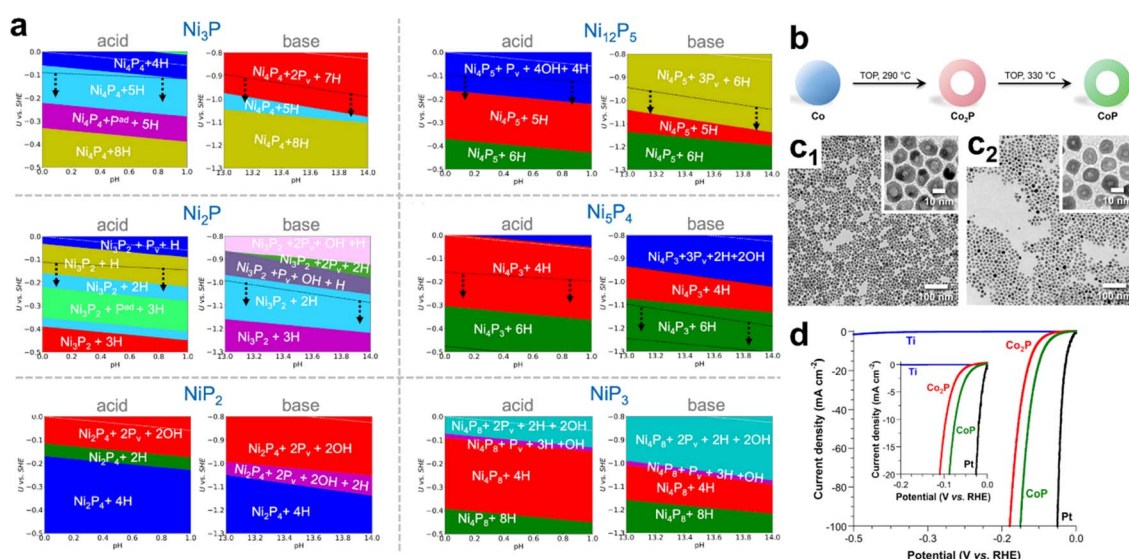


Fig. 5 (a) Surface phase diagrams illustrating surface termination and adsorbate (white letters), under electrochemical reaction conditions for Ni₃P, Ni₁₂P₅, Ni₂P, Ni₅P₄, NiP₂, and NiP₃. P_v: P vacancy; P_{ad}: P adatom. Boundary of bulk stability region and 0 V_{RHE} (RHE: reversible hydrogen electrode) lines are denoted by the dashed black and white lines, respectively. Reprinted with permission.¹¹⁹ 2023, American Chemical Society. (b) Schematic illustration of synthetic pathway for transforming Co nanoparticles into Co₂P and CoP nanoparticles. TEM images of (c₁) Co₂P and (c₂) CoP nanoparticles. (d) Polarization curves of Co₂P, CoP, Ti and Pt for HER in 0.5 M H₂SO₄. Reprinted with permission.⁵⁰ 2015, American Chemical Society.

Similarly, the influence of the composition of cobalt phosphides on the HER activity has been thoroughly investigated. Schaak's group synthesized Co_2P and CoP nanoparticles through the thermal decomposition of TOP, ensuring similar morphologies to directly compare their HER activities while minimizing other contributing factors (Fig. 5a, c_1 and c_2).⁵⁰ The observed trend in HER activity was $\text{Co} < \text{Co}_2\text{P} < \text{CoP}$, with CoP exhibiting the lowest overpotential, suggesting that a higher P content can lead to an increase in activity (Fig. 5d). Ha *et al.* further proposed, based on DFT results, that P could serve as an active site for the HER.³² This finding implied that a higher P content might enhance catalytic activity through different HER mechanisms occurring at P sites, distinct from traditional metal sites. The study also observed a gradual loss in activity, attributed to the formation of (oxy)phosphate(s) phases, as indicated by Co K-edge and P K-edge XAS results, which revealed the emergence of $\text{PO}_4(\text{P}^{5+})$ species. Xiao *et al.* demonstrated a correlation between the activity and stability of molybdenum phosphide and the degree of phosphorization.³⁴ They prepared Mo_3P and MoP through a two-step sintering process, where each sample underwent thermal treatment for 2 hours, Mo_3P at 800 °C under Ar and MoP at 650 °C under H_2 . Subsequent DFT calculations elucidated that post-phosphorization, the P site acted as an active site, displaying almost zero Gibbs free energy (ΔG_{H^*}). Consequently, MoP displayed superior electrocatalytic activity compared with those of Mo_3P and Mo. Moreover, Cho

et al. discovered that the phase-dependent HER activity of iron phosphide was $\text{Fe} < \text{Fe}_2\text{P} < \text{FeP}$.³³ While these comprehensive investigations have significantly advanced our understanding of the intricate relationships among composition, surface properties, and electrocatalytic performance in TMPs, it remains essential to conduct more deeper atomistic-level studies on the influence of P content, both for HER and OER catalysts.

5.2. Morphology/structure control

Many researchers have focused on augmenting the catalytic activity of TMPs *via* the meticulous control of their morphology. For instance, Chen *et al.* observed the dynamic microstructural changes in NiCoP , in which the structure evolved from hexagonal nanosheet arrays to nanoneedles based on hydrothermal temperature (90 to 150 °C) (Fig. 6a and b_{1-3}).¹⁰⁷ Synthesized at 120 °C, NiCoP exhibited a distinctive multiscale hierarchical structure, featuring nanoneedles that grew along the edges of nanosheets. This unique structure contributed to an increased active surface area, facilitating accelerated gas release and electron transfer. Consequently, this catalyst demonstrated high current density operation as a bifunctional catalyst with exceptional performance (1.981 V at 1 A cm^{-2}) and stable operation (600 h) (Fig. 6c). Similarly, Li *et al.* demonstrated a morphology-controllable synthesis of amorphous NiFeP nanostructures, displaying nanoparticles (NP), nanowires (NW),

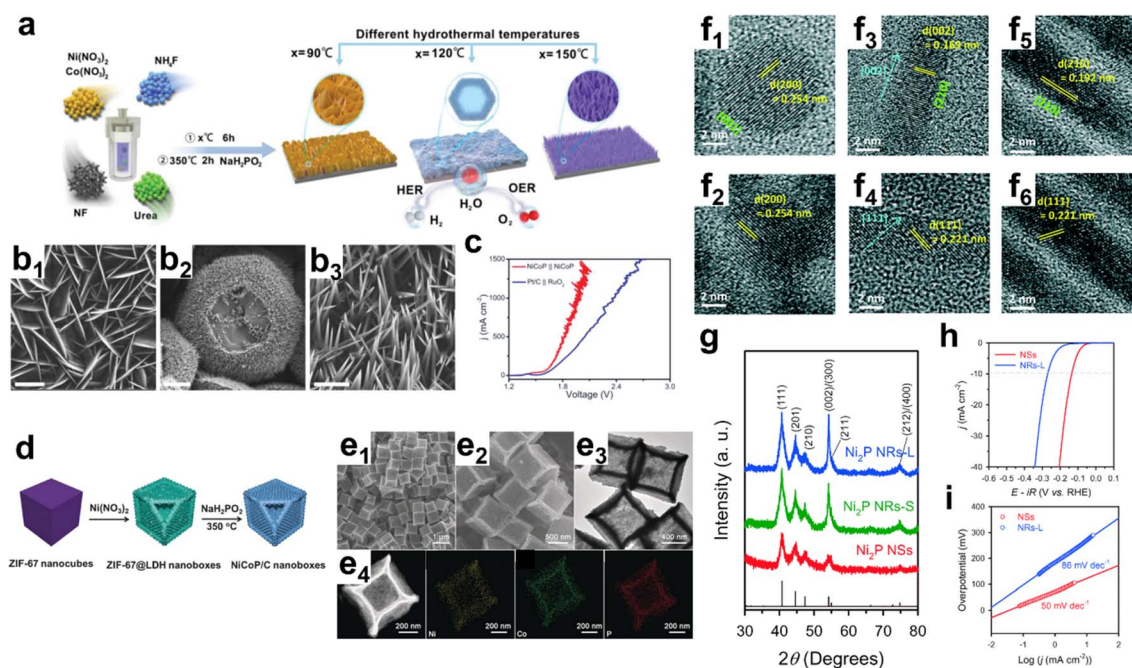


Fig. 6 (a) Schematic illustration of synthetic procedure of NiCoP . Scanning electron microscopy (SEM) images of NiCoP synthesized at hydrothermal temperature of (b₁) 90, (b₂) 120, and (b₃) 150 °C, respectively. The scale bars are 2, 5, and 2 μm in figure (b₁), (b₂), and (b₃), respectively. (c) Polarization curves of $\text{NiCoP}||\text{NiCoP}$ and $\text{Pt/C}||\text{RuO}_2$ electrodes for overall water splitting in alkaline media. Reprinted with permission.¹⁰⁷ 2023, John Wiley and Sons. (d) Schematic illustration for synthesizing NiCoP/C nanoboxes. (e₁ and e₂) SEM, (e₃) TEM, (e₄) high-angle annular dark-field scanning transmission electron microscopy (HAADF-STEM) and elemental mapping images of NiCoP nanoboxes. Reprinted with permission.¹²⁸ 2017, John Wiley and Sons. High resolution transmission electron microscopy (HRTEM) images of (f₁ and f₂) Ni_2P nanosphere (Ni_2P NSs), (f₃ and f₄) short nanorods (Ni_2P NRS-S), and (f₅ and f₆) long nanorods (Ni_2P NRS-L). (g) X-ray diffraction (XRD) patterns of as-synthesized Ni_2P NSs, Ni_2P NRS-S, and Ni_2P NRS-L. The vertical bars indicate the XRD pattern of the Ni_2P standard (JCPDS no. 89-2742). HER performance of Ni_2P NSs and Ni_2P NRS-L. (h) LSV curves and (i) Tafel plots. Reprinted with permission.¹²⁹ 2016, Royal Society of Chemistry.

nanosheets (NS) and thick flakes (TF), achieved by manipulating synthetic variables such as reaction time, temperature, and phosphorus source.¹¹¹ In alkaline simulated seawater, NiFeP-NS and NiFeP-NW performed well as HER and OER catalysts, requiring only 129 and 126 mV at 100 mA cm⁻², respectively. Consequently, this resulted in an overall water splitting voltage of 1.57 V at 100 mA cm⁻² (Table 1).

Metal-organic framework (MOF)-based synthesis strategies have been commonly used to control the morphology of TMPs. MOF-derived TMPs could exhibit various structures, including 0 D, 1 D, 2 D, and hollow structure, among others.¹⁴ For instance, Lou *et al.* successfully synthesized hollow NiCoP/C nanoboxes from Co-based ZIF-67 nanocubes (Fig. 6d), which had a uniform size of 750 nm, with each element (Ni, Co, and P) well-distributed throughout the shell of nanocubes (Fig. 6e₁₋₄), exhibiting higher activity in the alkaline OER than those of NiCoP and Ni-Co LDH.¹²⁸ Wang *et al.* prepared N-doped carbon-incorporated Mo-CoP nanosheet arrays on a Ti foil (Mo-CoP/NC/TF) using MOF-etching strategies.¹³⁰ When utilized as an HER catalyst, Mo-CoP/NC/TF displayed superior activity across all pH ranges, owing to its unique geometric structure.

The importance of shape control was further emphasized by several studies investigating the facet-dependent activity of TMPs. For instance, Schaak's group successfully synthesized highly branched CoP nanostructures that primarily exposed (111) crystal facets using chemical strategies involving a close relation between TOP and TOPO.⁵² However, these structures were less active than multi-faceted and spherical CoP NPs, requiring a higher overpotential of 117 mV compared to 100 mV for their counterparts to achieve a current density of 20 mA cm⁻². A similar study by Seo *et al.* involved the design of Ni₂P NPs in spherical shape (Ni₂P NSs) as well as in short rod and long rod shapes (Ni₂P NRS-S and NRS-L, respectively).¹²⁹ The Ni₂P NSs were prepared using a simple one-pot heat up method of Ni and P sources. The rod length was controlled by adjusting the injection rate of Ni-TOP

solution, with slower injection leading to the formation of longer nanorods. Their predominant crystal facets, identified by XRD and TEM characterization, were (001) for Ni₂P NSs and (210) for Ni₂P NRS-L, respectively (Fig. 6f₁₋₆). When used as HER catalysts, the Ni₂P NSs displayed higher activity and faster kinetics than the rod-shaped catalysts (Fig. 6h and i), indicating that an optimized shape with highly active crystal planes could substantially promote the catalytic activity of TMPs.

5.3. Interface engineering

Numerous studies have emphasized the pivotal role of the electronic structures of catalysts in catalytic processes.^{131,132} While adjusting the composition is an effective way to modulate electronic structure of monometallic TMPs, it often falls short of achieving significant improvements in catalytic activity. A more powerful approach to optimizing electronic structure is interface-engineering, which integrates different phases and simultaneously induces unprecedented properties owing to charge redistribution at hetero-interface region. For instance, to address the poor activity of metal-rich nickel phosphides, Zhou *et al.* employed an anion substitution strategy, integrating P-rich NiP₂ with Ni₅P₄ by substituting S with P through a solid-phase reaction.⁸⁷ This approach effectively constructed in-plane heterostructures and modulated the electronic structure between those of NiP₂ and Ni₅P₄. The formation of NiP₂/Ni₅P₄ heterojunction was clearly represented by HRTEM, where crystalline NiP₂ and Ni₅P₄ constructed a distinct boundary between them (Fig. 7a). Subsequent DFT calculations revealed that this electronic structure modulation resulted in hydrogen adsorption strength (ΔG_{H^*}) at the P site in the interface region approaching the ideal value (0 eV) (Fig. 7b and c). This optimization resulted in a catalytic performance comparable to that of Pt, achieving low overpotentials of 30 and 249 mV at 10 mA cm⁻² and 2 A cm⁻² for the acidic HER, respectively (Table 1).

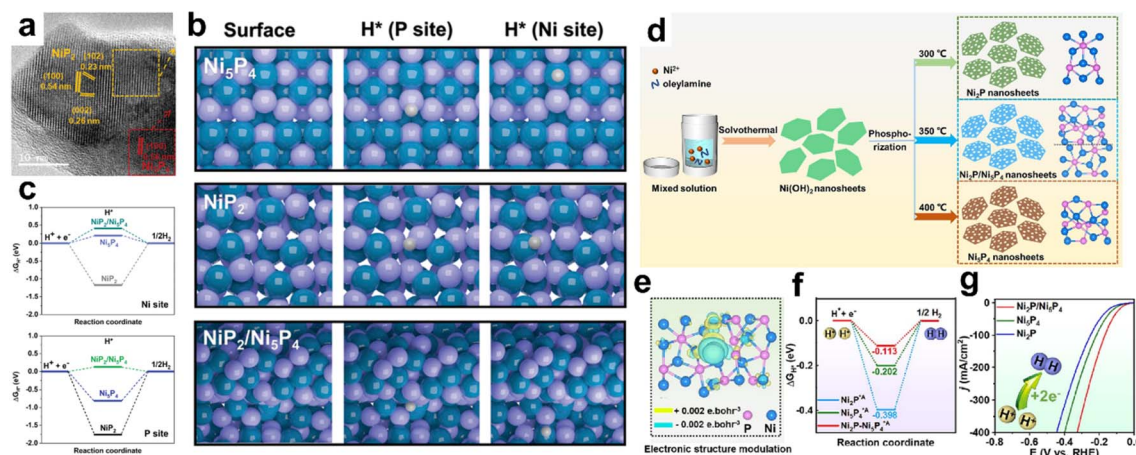


Fig. 7 (a) TEM image of in-plane NiP₂/Ni₅P₄ heterostructures. (b) Catalytic surface models with H adsorption on P and Ni sites of Ni₅P₄, NiP₂, and NiP₂/Ni₅P₄. Deep green: Ni; light blue: P; and gray: H. (c) ΔG_{H^*} calculated at equilibrium potential for HER at the Ni and P sites of the catalytic surfaces. Reprinted with permission.⁸⁷ 2022, John Wiley and Sons. (d) Schematic illustration of the preparation of Ni₂P, Ni₂P/Ni₅P₄, and Ni₅P₄ nanosheets. (e) Charge density at the interface of Ni₂P/Ni₅P₄ heterostructure nanosheets. (blue: depletion; yellow: accumulation) (f) Gibbs free energy diagram of Ni₂P, Ni₂P/Ni₅P₄, and Ni₅P₄ nanosheets. (g) HER polarization curves of Ni₂P, Ni₂P/Ni₅P₄, and Ni₅P₄ nanosheets in 0.5 M H₂SO₄. Reprinted with permission.⁵⁹ 2023, Elsevier.

Similarly, Lyu *et al.* developed Ni₂P/Ni₅P₄ heterostructured porous nanosheets *via* a solvothermal method followed by a phosphorization process, enabling a comparison of their activities with those of single-phase Ni₂P and Ni₅P₄ (Fig. 7d).⁵⁹ At the interface, the strong interaction between Ni₂P and Ni₅P₄ induced electron transfer from Ni₂P to Ni₅P₄ due to the difference in work function. This charge redistribution contributed to the optimization of the adsorption and desorption behaviors of reaction intermediates, resulting in improved HER activity of Ni₂P/Ni₅P₄ compared to the single-phase samples, with only 72 mV needed to reach 10 mA cm⁻² (Fig. 7e–g). Additionally, Yang *et al.* fabricated a NiSe₂/NiP₂ heterostructure through a one-step phosphoselenization of Ni(OH)₂ precursors to leverage the synergistic effects of combining the superior electrical conductivity of NiSe₂ with the exceptional stability of NiP₂.¹³⁵ The identical pyrite structures of NiP₂ and NiSe₂ exhibited a compatible lattice match, resulting in an interfacial strain of 4.3%. Such integration also brought about internal electron redistribution at the interface, as XPS revealed electron transfer from P to Se. Attributed to this electronic interaction, the NiSe₂/NiP₂ demonstrated accelerated water-splitting process, achieving a voltage of 1.56 V to deliver a current density of 10 mA cm⁻² in an assemble cell. Although current interfacial engineering strategies have yielded significant advancements in designing and promoting potential candidates to replace noble metal catalysts, challenges remain, such as understanding the atomistic configurations at the hetero-interface and their specific contributions to improved performance.

5.4. Defect engineering

Regulating electronic and band structure and active sites of TMPs can be realized by defect engineering, which consequently affects the catalytic behaviors.¹³⁶ For example, Yuan

et al. synthesized CoP nanorods with phosphorus vacancy (P_v) *via* NaBH₄ reduction of as-synthesized CoP.¹³³ After a 1 hour NaBH₄ treatment (referred to as CoP-B1), lattice defects were clearly visible in the HRTEM images, while the original morphology of the pristine CoP (referred to as CoP-B0) was retained (Fig. 8a and b). XPS analysis revealed that P_v altered the electronic structures of Co and P, with CoP-B1 showing a higher valence state of Co³⁺ compared to CoP-B0 (Co²⁺) (Fig. 8c). Additionally, the P 2p peaks also shifted to a lower energy level, although this shift was less pronounced than that observed in the Co 2p peaks, further indicating electron transfer from Co to P (Fig. 8d). Consequently, the anion deficiency in CoP-B1 facilitated the formation of phosphates species on its surface, and the higher valence state of Co promoted the reconstruction of active CoO_x(OH)_y sites, making CoP-B1 highly active as an OER catalyst. Using DFT calculations, Duan *et al.* explored the role of P_v in TMPs as catalysts for the HER and conducted a comparative analysis of the HER performance of Ni₁₂P₅ with and without P_v in an alkaline medium.¹³⁴ The Ni₁₂P₅ was synthesized *via* a solid-phase reaction by calcinating phosphate sources, and P_v was introduced by using an excess amount of P source. Owing to the P_v-induced electron redistribution, the energy barrier for the H*desorption step was significantly reduced, thereby improving the HER performance (Fig. 8f–h). Remarkably, the Ni₁₂P₅ with P_v (v-Ni₁₂P₅) displayed higher catalytic activity than pristine Ni₁₂P₅ (p-Ni₁₂P₅), even surpassing that of Pt/C (Fig. 8e). Ma *et al.* performed an analogous study on MoP and discovered that MoP with P_v exhibited a larger electrochemically active surface area and more favorable charge transfer, leading to the improved the HER activity in both acidic and alkaline electrolytes by up to 70 and 62 mV, respectively.¹³⁷

In addition to P vacancies, the introduction of cationic vacancies has been proven to be effective in modulating the

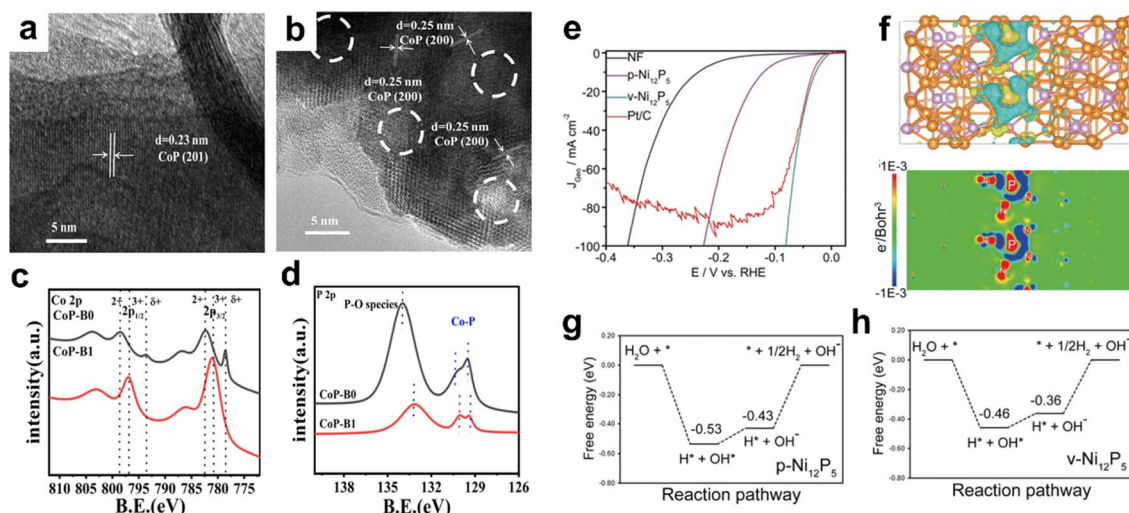


Fig. 8 HRTEM images of CoP (a) before NaBH₄ treatment (CoP-B0) and (b) after 1 h NaBH₄ treatment (CoP-B1), where some defects of the surface are circled by white dotted lines. XPS spectra of (c) Co 2p and (d) P 2p in CoP-B0 and CoP-B1. Reprinted with permission.¹³³ 2021, Elsevier. (e) Polarization curves for HER in 1 M KOH, comparing Ni₁₂P₅ with phosphorus vacancies (v-Ni₁₂P₅), pristine Ni₁₂P₅ (p-Ni₁₂P₅), nickel foam (NF), and Pt/C. (f) Electron distribution (cyan: electron depletion; yellow: electron accumulation) and two-dimensional charge density difference isosurface (red: electron accumulation; blue: electron depletion). Relative energy profiles of DFT calculated reaction pathways for (g) p-Ni₁₂P₅ and (h) v-Ni₁₂P₅. Reprinted with permission.¹³⁴ 2020, John Wiley and Sons.

electronic structure. Zhang *et al.* used Mn as a sacrificial dopant in Ni₂P, creating abundant vacancies through an acid-etching process of Mn in Ni₂P.¹³⁹ The introduction of cationic vacancies caused delocalization of electron around active Ni species and increased the valence state anionic P, as revealed by XPS analysis. Subsequent DFT calculations highlighted the relationship between cationic vacancy defects and enhanced catalytic activity, emphasizing changes in the Gibbs free energy of reaction intermediates in both the HER and OER processes.

More recently, a novel approach has been proposed that creating dual vacancies, both cationic and anionic, using a catalytically inactive phase. Xu *et al.* incorporated an inactive ZnO phase during the acid etching process of Ni foam, and then synthesized ZnO/Ni₂P heterostructure on Ni foam by a phosphorization process.⁹³ Although the ZnO phase did not participate directly in catalytic reactions, it served as an “electron pump”, withdrawing electrons from Ni and donating them to P. This process generated Ni cationic and P anionic vacancies, which in turn facilitated catalytic reactions, the highly oxidized Ni promoted hydrogen adsorption, while the P vacancies improved charge transfer, thereby enhancing overall catalytic performance.

5.5. Heteroatom doping

The incorporation of foreign elements into TMPs effectively modulates the local coordination and electronic structure of the

host material, influencing the surface affinity and, consequently, the electrochemical performance.¹⁴⁰ Numerous studies have demonstrated the crucial role of dopants in improving catalytic activity.^{141,142} For instance, Graves *et al.* conducted a computational study to explore the effects of various metal-dopants (M) on Ni₅P₄.¹³⁸ Their findings revealed that substituting the original Ni₃ hollow site on pristine Ni₅P₄, where hydrogen adsorption is most favorable, with Zn led to a significant contraction in the M–Ni bond length. This modification resulted in a Gibbs free energy (ΔG_{H^*}) close to zero, indicating enhanced hydrogen adsorption (Fig. 9b). Subsequent experimental studies, based on these theoretical calculations, successfully synthesized Ni_{5-x}Zn_xP nanocrystals and confirmed the superior HER performance of Ni_{4.90}Zn_{0.10}P₄, surpassing that of undoped Ni₅P₄ (Fig. 9a and c). Similarly, Lv *et al.* adopted a cation exchange technique to precisely control the doping amount and induced various defects at the surface, including lattice distortions and P vacancies.¹⁰⁸ HRTEM images and intensity profiles clearly demonstrated an increase in defects and phase development following the incorporation of Co into NiP (Fig. 9d–g). Electron energy loss spectroscopy (EELS) analysis further proved that P vacancies predominantly occurred near the Co sites on the outermost surface of the Ni_{0.96}Co_{0.04}P. Consequently, these surface-engineered Ni_{0.96}Co_{0.04}P catalysts exhibited significantly enhanced activity for overall water splitting compared to undoped NiP, highlighting the critical role of atomic-level engineering. The effect of lattice strain on

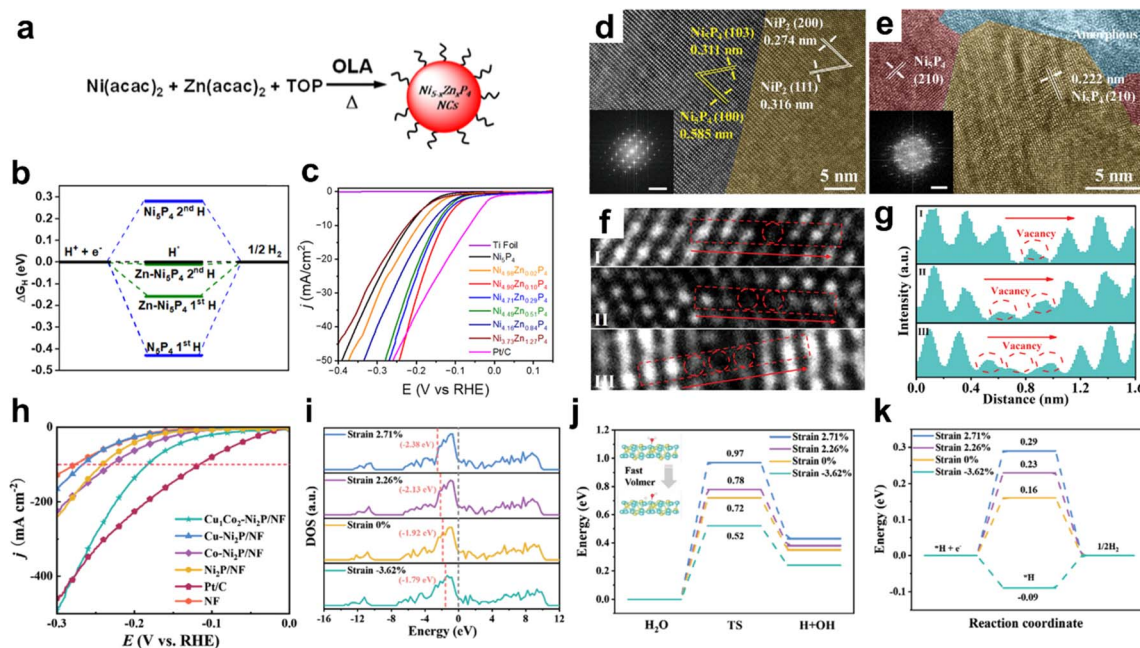


Fig. 9 (a) Schematic illustration for synthesizing Ni_{5-x}Zn_xP nanocrystals. (b) Gibbs free energy diagram of first and second hydrogen adsorptions for Ni₅P₄ and Zn-doped Ni₅P₄ (Zn-Ni₅P₄) (c) polarization curves of Ni_{5-x}Zn_xP, Ti foil, and Pt/C for HER in 1 M KOH. Reprinted with permission.¹³⁸ 2023, American Chemical Society. HRTEM images of (d) NiP and (e) Ni_{0.96}Co_{0.04}P. Inset: corresponding fast Fourier transform (FFT) pattern. (f) Atomic-scale view of Ni_{0.96}Co_{0.04}P, with phosphorus vacancies highlighted by red circles. (g) Intensity profile recoded from the corresponding areas in Fig. 2f. Reprinted with permission.¹⁰⁸ 2023, John Wiley and Sons. (h) HER polarization curves for Cu_xCo_y-Ni₂P/NF samples, Pt/C, and NF in 1.0 M KOH. (i) Comparison diagram of DOS, (j) energy barriers of water dissociation, and (k) ΔG_{H^*} for Ni₂P/NF, Cu_xCo_y-Ni₂P/NF, Co-Ni₂P/NF, and Cu-Ni₂P/NF with 0%, -3.62%, +2.26%, and +2.71% strains, respectively. The d-band center is denoted by pink dotted line. Reprinted with permission.⁹⁶ 2023, John Wiley and Sons.

the catalytic activity of Ni₂P induced by dual-cation co-doping was also reported by Feng *et al.*⁹⁶ They initially prepared Ni(OH)₂ doped with foreign metals (Cu and Co) on Ni foam, followed by phosphorization of this precursor through a gas-solid reaction using hypophosphite sources. When comparing the co-doped sample (Cu₁Co₂-Ni₂P/NF) with single metal-doped samples (Cu or Co-Ni₂P/NF), they found that the dual Co and Cu co-dopants induced a significant lattice compression of 3.62% and adjusted the d-band center closer to the Fermi level (Fig. 9i). Such strain facilitated rapid water dissociation and optimal adsorption/desorption of H* intermediates (Fig. 9j and k). As a result, the optimized Cu₁Co₂-Ni₂P/NF sample accomplished more than a two-fold improvement in the HER performance compared to Cu-Ni₂P/NF and Co-Ni₂P/NF (Fig. 9h). Similarly, an anion-cation co-doping strategy demonstrated by Zhu *et al.* enhanced the electrocatalytic properties with the ensemble effects of Zn and F ions.¹⁴³ Moreover, the introduction of nonmetal atoms alone into TMPs has been reported in various studies, including B-CoP nanowire arrays,⁹⁰ N-doped Ni-Co phosphide,¹⁴⁴ S-doped Co₂P,¹⁴⁵ and S-doped NiFeP driven by S-doped MOFs,¹⁰⁵ demonstrating the advantages of heteroatom doping on catalytic activity.

5.6. Alloying

The incorporation of additional elements is effective at overcoming the activity limitations of monometallic phosphides.

The positive impact of alloying on electrocatalytic properties has already been demonstrated in studies of transition metal sulfides (TMS).^{148,149} Shin *et al.* elucidated the alloying effect of TMPs by focusing solely on the alloy composition, excluding other variables.⁸⁸ They prepared Fe_xNi_{2-x}P samples with varying compositions *via* solution phase synthesis, while maintaining the same crystal structure of *P62m* as the monometallic phosphides (Ni₂P and Fe₂P) (Fig. 10a). Subsequent EXAFS analysis revealed significant distortion of Ni-P bonds and minimal distortion of the M-M bonds in Fe_{0.5}Ni_{1.5}P samples, attributed to alloying effects (Fig. 10b and c). These findings indicated that the reduced charge transfer from Ni to P might be responsible for the enhanced acidic HER activity. Habas *et al.* conducted a similar study to investigate the relationship between the electrocatalytic activity and the incorporation of secondary metal elements.¹⁴⁶ Using Ni₂P as the parent material, they synthesized alloyed nickel phosphides (Ni_{1.6}M_{0.4}P) by incorporating various metals (M = Co, Cu, Mo, Pd, Rh, and Ru) employing easily obtainable metal-phosphine precursors. All the synthesized samples maintained the same morphology and crystal structure as the host Ni₂P, with only slight lattice expansions, except for Ni_{1.6}Co_{0.4}P, allowing for direct comparison. Additionally, DFT calculations revealed that the adsorption free energy (*G*_H) varied with the different metal elements, leading to the successful establishment of a volcano-shaped relationship between composition and catalytic activity

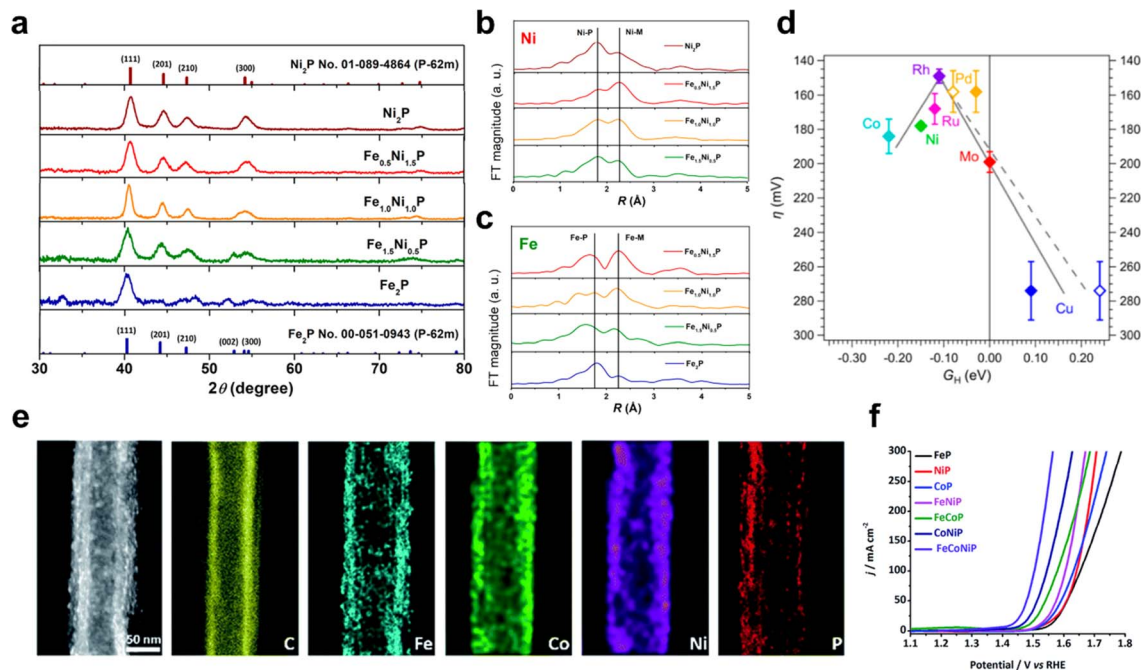


Fig. 10 (a) XRD patterns of Fe_{2-x}Ni_xP. Vertical bars indicate the Ni₂P (top) and Fe₂P (bottom) reference, respectively. Fourier transformed extended X-ray absorption fine structure (EXAFS) spectra of (b) Ni k-edge and (c) Fe k-edge for Fe_{2-x}Ni_xP. Reprinted with permission.⁸⁸ 2020, American Chemical Society. (d) Volcano plot showing the overpotential as a function of Gibbs free energy for hydrogen adsorption on ABB-terminated Ni_{1.67}M_{0.33}P(10 $\bar{1}$ 0) surfaces (solid markers) and Cu- and Pd-enriched Ni_{1.33}M_{0.67}P(10 $\bar{1}$ 0) surfaces (open markers). The gray lines illustrate the relationship between η and *G*_H for Ni_{1.67}M_{0.33}P(10 $\bar{1}$ 0) surfaces alone (solid) and when including Cu- and Pd-enriched surfaces (dashed). Reprinted with permission.¹⁴⁶ 2022, American Chemical Society. (e) Scanning transmission electron microscopy (STEM) image and the corresponding elemental mappings of FeCoNiP catalyst. (f) Comparison of oxygen evolution reaction performance for various transition metal phosphides. Reprinted with permission.¹⁴⁷ 2018, Royal Society of Chemistry.

(Fig. 10d). Other synthetic methods for obtaining bimetallic phosphides included the conversion of a core/shell structure to a solid solution through an annealing process, which could overcome the limitations of conventional method that often yielded uncontrollable nanostructures.¹⁰⁶ Additionally, electro-deposition techniques also could be employed to fabricate alloyed TMPs film with hierarchical morphologies.¹⁵⁰

Trimetallic phosphides have demonstrated higher catalytic activities compared to their mono- and bi-metallic counterparts. Liu *et al.* synthesized different compositions of TMPs through a solution-based chemical reduction of metal ions, followed by phosphorization of the resulting powders *via* a gas-solid reaction.¹⁴⁷ These TMPs were characterized by a uniform distribution of each element, and their catalytic performances were thoroughly investigated (Fig. 10e). The OER performance followed the sequence FeP < NiP < CoP < FeNiP < CoNiP < FeCoP < CoNiP < FeCoNiP, which corresponded to the inclination observed in the chemical shift of metal–P bonds in XPS spectra (Fig. 10f). This gradual increase in catalytic activity clearly highlighted the importance of the high valence states of metal species induced by alloying effects. Similarly, Kumar *et al.* reported that spikey-ball-shaped FeCoNiP exhibited superior activity as water-splitting catalysts at an industrial scale level.¹⁰⁹ Using a one-pot heat-up method with metal and P precursors, they controlled the composition of the products by adjusting the ratio of metal precursors. Their results showed that Fe_{0.5}-CoNi_{0.5}P displayed the highest catalytic activity, implying that this synthetic strategy holds promise for practical applications. Additionally, MOF-based methods could be used to synthesize ternary TMPs. For instance, Li *et al.* synthesized MOF-derived Ni-Co-Fe-P nanobricks and demonstrated exceptional performance, achieving a high activity of 1.46 V at 10 mA cm⁻² (Table 1) while maintaining stable operation at an industrial-level current density toward overall water splitting.¹¹⁰ Furthermore, TMPs alloyed with various combinations of elements have been reported, including Mn–Ni–Co ternary phosphides,¹⁵⁴ quaternary Ni–Co–S–P,¹⁵⁵ and Zn–Ni–Co–M (M = O, S, P, and Se).¹⁵⁶

5.7. High-entropy TMPs

High-entropy materials, which consist of more than five uniformly mixed elements in a single-phase, have recently attracted widespread attention.^{157,158} Despite the inherent challenges associated with mixing multiple elements, such as phase separation and irregular elemental distribution, numerous studies have shown that through various synthetic strategies, it is possible to achieve a complete solid solution in high-entropy alloys (HEAs) thereby modulating their physicochemical properties. This phenomenon is particularly evident in high-entropy transition metal phosphides (HEMPs), where the synergistic effects of individual elements give rise to unique characteristics not previously observed in simpler systems. A notable example is the work by Zhao *et al.*, where five metal chloride precursors and tetrabutylphosphonium chloride (TBPC) were combined with ethylene glycol (EG) as a eutectic solvent.¹⁵⁹ The mixture was then thermally treated at 400 °C under a N₂ atmosphere. This eutectic solvent method successfully yielded HEMPs

containing Co, Cr, Mn, Fe, Ni, and P. Remarkably, these HEMPs exhibited significantly enhanced HER and OER performances compared to their monometallic phosphide counterparts. This study not only introduced a novel synthetic approach for HEMPs but also highlighted the potential for expanding the compositional diversity and functional capabilities of these materials by incorporating additional elements through the simple mixing of different metal chloride sources. Using a sol-gel synthetic method, Lu *et al.* further demonstrated the synergistic effects of the metal elements mentioned above by comparing the electrocatalytic activity of single-phase TMPs with varying compositions, ranging from mono- to multi-metallic phosphides (Fig. 11a).¹⁵¹ Their findings revealed that HER and OER performance improved with an increase in the number of metal ions, likely due to electronic structure modulation induced by increased entropy (Fig. 11b and c). In another approach, Li *et al.* electrodeposited a CoFeNiCrMnP compound on NF, providing a different method for synthesizing HEMPs and identified the role of each metal element in the HER process.⁶⁴ Comparative analysis with quaternary TMPs confirmed the superior activity and kinetics of CoFeNiCrMnP in catalytic reactions, with Fe and Ni making particularly significant contributions to hydrogen evolution (Fig. 11d and e). This work suggests that a detailed analysis in individual elements within HEMPs could lead to further enhancements in catalytic performance through optimized compositional design. Wang *et al.* clearly showed enhanced HER performance by high-entropy effect, as confirmed by DFT calculations.¹⁵² The solid-state reaction using each element powder and subsequent exfoliation process produced 2D Co_{0.6}(VMnNiZn)_{0.4}PS₃ nano-sheets, achieving notable catalytic activity (65.9 mV@10 mA cm⁻²). Theoretical studies demonstrated that in high-entropy materials (CoVMnNiZnPS₃), the edge S sites and basal P sites were more active than metal Co sites, with optimized ΔG_{H^+} values of -0.17 eV and 0.35 eV for HE-S and HE-P, respectively (Fig. 11f and g). Additionally, Mn sites in Co_{0.6}(VMnNiZn)_{0.4}PS₃ exhibited a lower water dissociation barrier (0.69 eV) than Co sites in CoPS₃ (1.21 eV), demonstrating promoted kinetics in the Volmer step for alkaline HER, attributed to the high-entropy effect (Fig. 11h). To further enhance electrocatalytic performance, recent efforts have focused on synthesizing HEMPs with controlled crystal structures or unique morphologies. A novel synthetic method of using a high-entropy MOF (HE-MOF) as the template resulted in short-range amorphous FeCoNiCuMnP_x/C composites, which ensured high electron conductivity and abundant reaction sites.¹⁶⁰ Furthermore, Du *et al.* developed the comelting-filling-freezing-modification (co-MFFM) method to synthesize 1D high-entropy metal phosphides encapsulated by single-wall carbon nanotubes (HEP@SWNTs), which offered superior activity owing to efficient mass transfer and stable operation as electrocatalysts (Fig. 11i and j).¹⁵³ Although the detailed effects of alloying with various metals on the modification of the electronic structures have not been fully elucidated, these studies present notable synthetic strategies with distinct advantages and may help gain diverse perspectives on the approach and development of HEMPs.

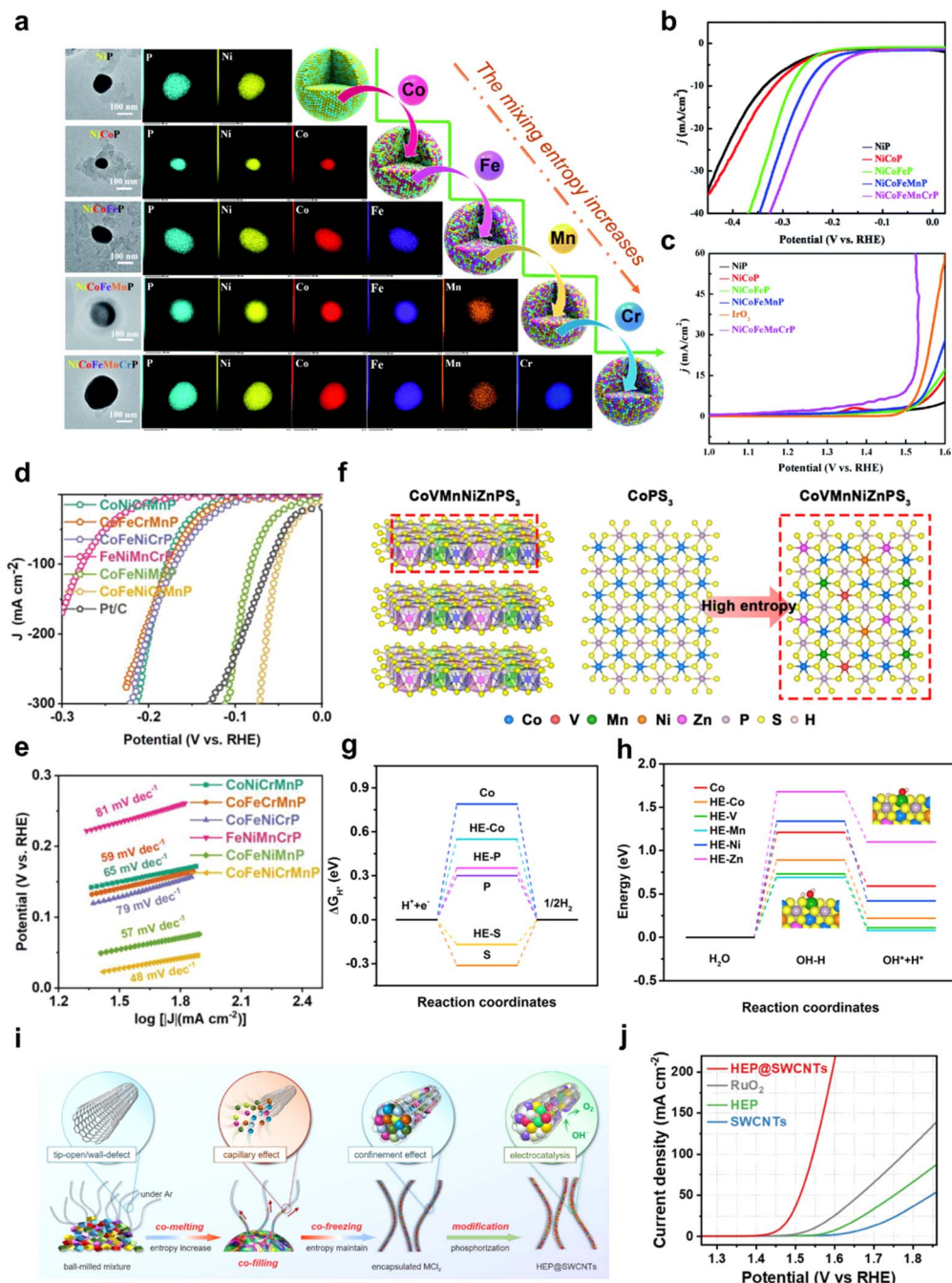


Fig. 11 (a) TEM and element mapping images of obtained TMP nanoparticles. Polarization curves for (b) HER and (c) OER of different electrocatalysts in 1.0 M KOH. Reprinted with permission.¹⁵¹ 2021, Royal Society of Chemistry. (d) Polarization curves and (e) Tafel plots for HER of high entropy catalysts in 1 M KOH solution. Reprinted with permission.⁶⁴ 2023, John Wiley and Sons. (f) Crystal structure of CoVMnNiZnPS₃ and top views of CoPS₃ and CoVMnNiZnPS₃, respectively. (g) Free energy diagram for HER at the edge sites. (h) Calculated energy profiles of water dissociation for Co_{0.6}(VMnNiZn)_{0.4}PS₃ and CoPS₃, including Co, V, Mn, Ni, and Zn sites. Reprinted with permission.¹⁵² 2022, American Chemical Society. (i) The synthetic procedure for HEP@SWCNTs. (j) LSV curves of HEP@SWCNTs, RuO₂, HEP, and SWCNTs for OER in 1 M KOH. Reprinted with permission.¹⁵³ 2024, American Chemical Society.

6. Conclusion and outlooks

In this review, a comprehensive discussion of the fundamental aspects and evaluation parameters of HER and OER was presented. Moreover, the origin of the activity of TMPs was described in terms of the role of P and theoretical descriptors,

such as the Gibbs free energy. Subsequently, various P sources and synthetic strategies including conventional methods and novel approaches were introduced. Finally, numerous studies on the activity enhancement strategies of TMPs and their corresponding impacts on performance were summarized. As substantial achievements have been made in the electrolysis

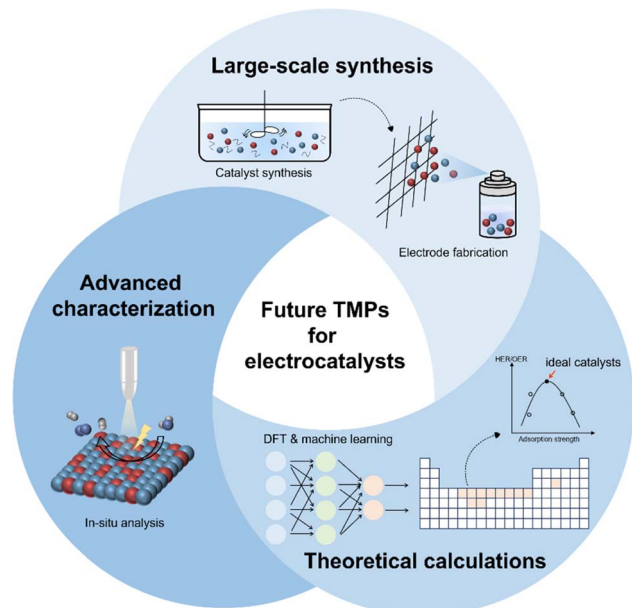


Fig. 12 Schematic illustration of outlooks for future TMPs.

applications of TMPs, the electronic structure, microstructure, and adsorption/desorption strength of the reaction intermediates were revealed to be the primary factors influencing the electrocatalytic properties.

Despite the substantial achievements indicating the exceptional HER and OER performances of TMPs, comparable with those of noble metal-based electrocatalysts, there is still room for improvement to fully replace commercially used catalysts. The following improvements are suggested (Fig. 12).

(1) For industrial-scale applications, it is essential to develop large-scale synthesis methods and electrode fabrication processes. While lab-scale experiments, conducted under ideal conditions, have demonstrated the exceptional performance and stability of TMPs, few studies have explored their use in actual water-splitting devices. Given the practical applications, such as proton exchange membrane and anion exchange membrane water electrolyzer (PEMWE/AEMWE), operate under relatively harsh conditions like high temperature (~ 80 °C) and operation voltage and current density, it is important to develop simple, scalable synthetic strategies that maintain activity and stability in such environments.

The synthesis of TMPs at the laboratory scale is currently hampered by significant limitations that must be addressed to enable large-scale production. Conventional synthetic methods typically require high reaction temperatures and often produce toxic gases, such as PH_3 , due to the use of large quantities of elemental P or hypophosphite compounds. These challenges pose significant barriers to both the scalability and environmental sustainability of TMP production.

In response to these current issues, recent efforts have focused on developing green and economically viable large-scale synthesis methods. Among the most promising approaches is the use of phytic acid and biomass, such as (*Saccharomyces*/yeasts), as environmentally friendly and cost-effective P sources.

Successful synthesis of various TMPs using these green methods has been reported, suggesting a viable pathway towards sustainable large-scale production. Additionally, ink-jet printing using ionic liquid P sources, such as $[\text{BMIM}]\cdot\text{PF}_6$, has emerged as another potential technique for large-scale fabrication, achieving production dimensions up to 10×10 cm².

In practical applications, particularly for colloidal TMPs particles, the choice of film fabrication methods is also crucial, as these devices typically require either a catalyst-coated substrate (CCS) or a catalysts-coated membrane (CCM). For example, common methods like spray coating and drop casting offer simple and fast processing, while electrophoretic deposition (EPD) can produce catalysts film with strong adherence, enhancing stability during catalytic reactions. To abbreviate these film fabrication process, self-supported electrodes have been predominantly developed, such as those produced *via* electrodeposition and hydrothermal reactions. These methods enable the direct growth of catalysts materials on substrates, such as Ni foam or carbon paper, resulting in 3D structures with large surface areas and porous architectures that promote efficient water electrolysis. Furthermore, designing substrates with unique structures or robust properties than conventional ones can further enhance catalytic performance and durability, underscoring the necessity of ongoing research.

(2) The development and application of advanced, diverse characterization techniques are crucial for gaining deeper insights into the behavior of high-entropy transition metal phosphides (TMPs) in electrocatalysis. While the strategy of combining various elements has significantly improved electrocatalytic performance, the precise contribution of each element remains ambiguous, particularly in complex high-entropy TMPs systems. A key challenge arises from the inevitable surface reconstruction that TMP catalysts undergo under electrochemical conditions. This process often leads to changes in surface morphology, crystal structure, and electronic properties. For examples, it is widely recognized that during OER, the surface of TMPs transforms into layers of metal oxides, hydroxides, or oxyhydroxides, which serve as the active sites for catalysis. Therefore, detailed analyses are essential to elucidate the role of each metal element in TMPs and to design optimized catalysts using these expected transformations.

In situ XAS has emerged as a vital tool for monitoring changes in oxidation states and bond-lengths, enabling comparison with *ex situ* analyses and aiding in the identification of active electrocatalyst. *In situ* Raman technique can also provide valuable insights into the concomitant formation of oxygen-coordinated species, further elucidating the contributions of practical metal species during electrochemical reactions. Similarly, isotope-labelling method using H_2^{16}O and H_2^{18}O solution has been widely used to determine the reaction pathway of AEM or LOM during OER process, in conjunction with *in situ* infrared (IR) spectroscopy. This combination allows researchers to measure surface-adsorbed oxygen species, helping to identify reaction mechanisms and active metal sites. Additionally, *in situ* TEM is particularly advantageous for observing the structural evolution of catalysts under applied

potentials, during long-term operation, or even throughout the synthesis process.

Despite the advancements in *in situ* characterization techniques, there remains a need for more advanced methodologies capable of achieving atomic resolution for in-depth understanding. Such technologies are essential for an in-depth understanding of the intricate processes that occur, ultimately guiding the design of more efficient and stable electrocatalysts.

(3) Although computational calculations offer meaningful information to predict active sites and their corresponding activities through a simulation model, they do not fully mirror what happens in the actual electrochemical environments. Therefore, it is important to bridge the gap between computational predictions and real-world electrochemical reactions.

To achieve a more precise understanding, well-organized simulation models that closely resemble structures under practical electrochemical environments can be developed based on *in situ* analysis results, taking predicted surface reconstruction into account. These models enable to provide significant insights, such as the role of P atoms, intermetallic interactions in multi-metallic TMPs, and more accurate results that align closely with experimental findings.

Additionally, machine learning (ML), another powerful theoretical approach, has increasingly been used to figure out ideal compositions and structural candidates for TMPs, substantially reducing the time required for experimental exploration. For instance, ML can suggest optimal combinations of metal species for HEMPs catalysts or propose entirely new approaches to TMPs, potentially paving the way for innovative advancements.

Therefore, ongoing exploration of innovative synthetic methods and material characterization, along with a deep understanding of catalytic reaction mechanisms holds significant potential for the developing efficient, green and cost-effective water-splitting catalysts that can be applied as practical devices.

Data availability

No primary research results, software or code have been included and no new data were generated or analyzed as part of this review.

Author contributions

Yeongbin Lee & Wooseok Jeong: conceptualization, investigation, writing – original draft, and writing – review and editing. Yun Jae Hwang & Boeun An: data curation, investigation, and visualization. Hyeonseok Lee: data curation and visualization. Heesoo Jeong: investigation and visualization. Gyuhyeon Kim & Yoonsu Park: validation. Minyoung Kim: investigation. Don-Hyung Ha: conceptualization, funding acquisition, project administration, supervision, writing (original draft), and writing (review and editing).

Conflicts of interest

There are no conflicts to declare.

Acknowledgements

This review was supported by the National Research Foundation of Korea (NRF) grant funded by the Korean government (MSIT) (grant number: 2020R1A5A1018052/RS-2023-00255695). This research was supported by the Chung-Ang University Graduate Research Scholarship in 2023.

References

- Z. W. Seh, J. Kibsgaard, C. F. Dickens, I. Chorkendorff, J. K. Nørskov and T. F. Jaramillo, *Science*, 2017, **355**, eaad4998.
- Z.-Y. Wu, F.-Y. Chen, B. Li, S.-W. Yu, Y. Z. Finprock, D. M. Meira, Q.-Q. Yan, P. Zhu, M.-X. Chen, T.-W. Song, Z. Yin, H.-W. Liang, S. Zhang, G. Wang and H. Wang, *Nat. Mater.*, 2023, **22**, 100–108.
- K. Mazloomi and C. Gomes, *Renewable Sustainable Energy Rev.*, 2012, **16**, 3024–3033.
- W. Lubitz and W. Tumas, *Chem. Rev.*, 2007, **107**, 3900–3903.
- Y. Jiao, Y. Zheng, M. Jaroniec and S. Z. Qiao, *Chem. Soc. Rev.*, 2015, **44**, 2060–2086.
- C. C. Pavel, F. Cecconi, C. Emiliani, S. Santiccioli, A. Scaffidi, S. Catanorchi and M. Comotti, *Angew. Chem., Int. Ed.*, 2014, **53**, 1378–1381.
- Y. Zheng, A. Serban, H. Zhang, N. Chen, F. Song and X. Hu, *ACS Energy Lett.*, 2023, **8**, 5018–5024.
- M. Kim, H. Kang, E. Hwang, Y. Park, W. Jeong, Y. J. Hwang and D.-H. Ha, *Appl. Surf. Sci.*, 2023, **612**, 155862.
- Y. Park, H. Kim, T. Lee, Y.-K. Hong, W. Jeong, S.-K. Kim and D.-H. Ha, *Chem. Eng. J.*, 2022, **431**, 133217.
- W. Wu, X. Ma, Y. Zhu, F. Hu, G. Huang, N. Wang, S. Ning, Y. Zhu, P. Kang Shen and J. Zhu, *Chem. Eng. J.*, 2023, **478**, 147425.
- D. V. Esposito, S. T. Hunt, Y. C. Kimmel and J. G. Chen, *J. Am. Chem. Soc.*, 2012, **134**, 3025–3033.
- J. Wang, S.-J. Kim, J. Liu, Y. Gao, S. Choi, J. Han, H. Shin, S. Jo, J. Kim, F. Ciucci, H. Kim, Q. Li, W. Yang, X. Long, S. Yang, S.-P. Cho, K. H. Chae, M. G. Kim, H. Kim and J. Lim, *Nat. Catal.*, 2021, **4**, 212–222.
- X. Li, W. Xing, T. Hu, K. Luo, J. Wang and W. Tang, *Coord. Chem. Rev.*, 2022, **473**, 214811.
- L.-M. Cao, J. Zhang, L.-W. Ding, Z.-Y. Du and C.-T. He, *J. Energy Chem.*, 2022, **68**, 494–520.
- H. H. Do, M. A. Tekalgne, Q. V. Le, J. H. Cho, S. H. Ahn and S. Y. Kim, *Nano Convergence*, 2023, **10**, 6.
- H. Huang, L. Xu, D. Yoon Woo, S. Kim, S. Min Kim, Y. Kyeong Kim, J. Byeon and J. Lee, *Chem. Eng. J.*, 2023, **451**, 138939.
- Z. Pu, T. Liu, I. S. Amiin, R. Cheng, P. Wang, C. Zhang, P. Ji, W. Hu, J. Liu and S. Mu, *Adv. Funct. Mater.*, 2020, **30**, 2004009.
- C.-C. Weng, J.-T. Ren and Z.-Y. Yuan, *ChemSusChem*, 2020, **13**, 3357–3375.
- F. Lu, M. Zhou, Y. Zhou and X. Zeng, *Small*, 2017, **13**, 1701931.

- 20 A. Karmakar, S. Nagappan, A. Das, A. Kalloorkal and S. Kundu, *J. Mater. Chem. A*, 2023, **11**, 15635–15642.
- 21 Y. Zhao, N. Dongfang, C. A. Triana, C. Huang, R. Erni, W. Wan, J. Li, D. Stoian, L. Pan, P. Zhang, J. Lan, M. Iannuzzi and G. R. Patzke, *Energy Environ. Sci.*, 2022, **15**, 727–739.
- 22 Y. Zhao, D. P. Adiyeri Saseendran, C. Huang, C. A. Triana, W. R. Marks, H. Chen, H. Zhao and G. R. Patzke, *Chem. Rev.*, 2023, **123**, 6257–6358.
- 23 A. Kerschbaumer, D. Wielend, E. Leeb, C. Schimanofsky, N. Kleinbruckner, H. Neugebauer, M. Irimia-Vladu and N. S. Sariciftci, *Catal. Sci. Technol.*, 2023, **13**, 834–843.
- 24 Y. Shi and B. Zhang, *Chem. Soc. Rev.*, 2016, **45**, 1529–1541.
- 25 Y. Luo, Z. Zhang, M. Chhowalla and B. Liu, *Adv. Mater.*, 2022, **34**, 2108133.
- 26 Y. Wang, D. Dang, D. Li, J. Hu, X. Zhan and Y.-T. Cheng, *J. Power Sources*, 2019, **438**, 226938.
- 27 W. Jeong, Y. Park, Y.-K. Hong, I. Kim, H. Son and D.-H. Ha, *J. Phys. Chem. Lett.*, 2023, **14**, 1230–1238.
- 28 J. H. Prosser, T. Brugarolas, S. Lee, A. J. Nolte and D. Lee, *Nano Lett.*, 2012, **12**, 5287–5291.
- 29 D. Kim, X. Qin, B. Yan, H. Hong and Y. Piao, *ACS Appl. Energy Mater.*, 2020, **3**, 9769–9784.
- 30 D. Kim, X. Qin, B. Yan and Y. Piao, *Chem. Eng. J.*, 2021, **408**, 127331.
- 31 Y. Li, K. Li, L. Li, J. Gao, Z. Wang, W. Zou, H. Li, Q. Zhang, Y. Li, X. Zhang, D. Tian and L. Jiang, *Adv. Mater.*, 2024, 2405493.
- 32 D.-H. Ha, B. Han, M. Risch, L. Giordano, K. P. C. Yao, P. Karayaylali and Y. Shao-Horn, *Nano Energy*, 2016, **29**, 37–45.
- 33 G. Cho, H. Kim, Y. S. Park, Y.-K. Hong and D.-H. Ha, *Int. J. Hydrogen Energy*, 2018, **43**, 11326–11334.
- 34 P. Xiao, M. A. Sk, L. Thia, X. Ge, R. J. Lim, J.-Y. Wang, K. H. Lim and X. Wang, *Energy Environ. Sci.*, 2014, **7**, 2624–2629.
- 35 Y. Pan, Y. Liu, J. Zhao, K. Yang, J. Liang, D. Liu, W. Hu, D. Liu, Y. Liu and C. Liu, *J. Mater. Chem. A*, 2015, **3**, 1656–1665.
- 36 A. Ray, S. Sultana, L. Paramanik and K. M. Parida, *J. Mater. Chem. A*, 2020, **8**, 19196–19245.
- 37 D. Liu, G. Xu, H. Yang, H. Wang and B. Y. Xia, *Adv. Funct. Mater.*, 2023, **33**, 2208358.
- 38 P. W. Menezes, A. Indra, C. Das, C. Walter, C. Göbel, V. Gutkin, D. Schmeißer and M. Driess, *ACS Catal.*, 2017, **7**, 103–109.
- 39 R. Liu, T. Song, H. Xue, J. Sun, N. Guo, J. Sun, Y.-R. Hao and Q. Wang, *ACS Appl. Energy Mater.*, 2023, **6**, 692–701.
- 40 J. Mao, J. Kang, W. Wang, Q. Zhang, Y. Shao and J. Yuan, *Electrochim. Acta*, 2024, **503**, 144906.
- 41 W. Wu, S. Luo, Y. Huang, H. He, P. K. Shen and J. Zhu, *Mater. Chem. Front.*, 2024, **8**, 1064–1083.
- 42 X. Han, C. Yu, Y. Niu, Z. Wang, Y. Kang, Y. Ren, H. Wang, H. S. Park and J. Qiu, *Small Methods*, 2020, **4**, 2000546.
- 43 R. Luo, Z. Qian, L. Xing, C. Du, G. Yin, S. Zhao and L. Du, *Adv. Funct. Mater.*, 2021, **31**, 2102918.
- 44 F. Ye, Y. Cao, W. Han, Y. Yang, Y. Feng, P. Liu, C. Xu, X. Du, W. Yang and G. Liu, *Korean J. Chem. Eng.*, 2022, **39**, 596–604.
- 45 R. Gao, L. Pan, H. Wang, X. Zhang, L. Wang and J.-J. Zou, *ACS Catal.*, 2018, **8**, 8420–8429.
- 46 J. Ren, J.-g. Wang, J.-f. Li and Y.-w. Li, *J. Fuel Chem. Technol.*, 2007, **35**, 458–464.
- 47 P. Liu and J. A. Rodriguez, *Catal. Lett.*, 2003, **91**, 247–252.
- 48 A. J. Medford, A. Vojvodic, J. S. Hummelshøj, J. Voss, F. Abild-Pedersen, F. Studt, T. Bligaard, A. Nilsson and J. K. Nørskov, *J. Catal.*, 2015, **328**, 36–42.
- 49 J. Kibsgaard, C. Tsai, K. Chan, J. D. Benck, J. K. Nørskov, F. Abild-Pedersen and T. F. Jaramillo, *Energy Environ. Sci.*, 2015, **8**, 3022–3029.
- 50 J. F. Callejas, C. G. Read, E. J. Popczun, J. M. McEnaney and R. E. Schaak, *Chem. Mater.*, 2015, **27**, 3769–3774.
- 51 E. J. Popczun, C. G. Read, C. W. Roske, N. S. Lewis and R. E. Schaak, *Angew. Chem., Int. Ed.*, 2014, **53**, 5427–5430.
- 52 E. J. Popczun, C. W. Roske, C. G. Read, J. C. Crompton, J. M. McEnaney, J. F. Callejas, N. S. Lewis and R. E. Schaak, *J. Mater. Chem. A*, 2015, **3**, 5420–5425.
- 53 E. J. Popczun, J. R. McKone, C. G. Read, A. J. Biacchi, A. M. Wiltrout, N. S. Lewis and R. E. Schaak, *J. Am. Chem. Soc.*, 2013, **135**, 9267–9270.
- 54 J. M. McEnaney, J. Chance Crompton, J. F. Callejas, E. J. Popczun, C. G. Read, N. S. Lewis and R. E. Schaak, *Chem. Commun.*, 2014, **50**, 11026–11028.
- 55 A. E. Henkes, Y. Vasquez and R. E. Schaak, *J. Am. Chem. Soc.*, 2007, **129**, 1896–1897.
- 56 Y. Park, H. Kang, Y.-k. Hong, G. Cho, M. Choi, J. Cho and D.-H. Ha, *Int. J. Hydrogen Energy*, 2020, **45**, 32780–32788.
- 57 H. Zhang, D.-H. Ha, R. Hovden, L. F. Kourkoutis and R. D. Robinson, *Nano Lett.*, 2011, **11**, 188–197.
- 58 J. Xu, Y. Liu, J. Li, I. Amorim, B. Zhang, D. Xiong, N. Zhang, S. M. Thalluri, J. P. S. Sousa and L. Liu, *J. Mater. Chem. A*, 2018, **6**, 20646–20652.
- 59 C. Lyu, C. Cao, J. Cheng, Y. Yang, K. Wu, J. Wu, W.-M. Lau, P. Qian, N. Wang and J. Zheng, *Chem. Eng. J.*, 2023, **464**, 142538.
- 60 J. Chi, L. Guo, J. Mao, T. Cui, J. Zhu, Y. Xia, J. Lai and L. Wang, *Adv. Funct. Mater.*, 2023, **33**, 2300625.
- 61 J. Shi, W. Peng, Y.-F. Yang, B. Li, J. Nie, H. Wan, Y. Li, G.-F. Huang, W. Hu and W.-Q. Huang, *Small*, 2023, **19**, 2302906.
- 62 H. Liang, A. N. Gandi, D. H. Anjum, X. Wang, U. Schwingenschlögl and H. N. Alshareef, *Nano Lett.*, 2016, **16**, 7718–7725.
- 63 H. Zhang, D. J. Hagen, X. Li, A. Graff, F. Heyroth, B. Fuhrmann, I. Kostanovskiy, S. L. Schweizer, F. Caddeo, A. W. Maijenburg, S. Parkin and R. B. Wehrspohn, *Angew. Chem., Int. Ed.*, 2020, **59**, 17172–17176.
- 64 K. Li, J. He, X. Guan, Y. Tong, Y. Ye, L. Chen and P. Chen, *Small*, 2023, **19**, 2302130.
- 65 F. Yao, M. Jia, Q. Yang, F. Chen, Y. Zhong, S. Chen, L. He, Z. Pi, K. Hou, D. Wang and X. Li, *Water Res.*, 2021, **193**, 116881.
- 66 Z. Pu, Q. Liu, A. M. Asiri and X. Sun, *ACS Appl. Mater. Interfaces*, 2014, **6**, 21874–21879.

- 67 J. Jiang, C. Wang, J. Zhang, W. Wang, X. Zhou, B. Pan, K. Tang, J. Zuo and Q. Yang, *J. Mater. Chem. A*, 2015, **3**, 499–503.
- 68 W. Zhang, N. Han, J. Luo, X. Han, S. Feng, W. Guo, S. Xie, Z. Zhou, P. Subramanian, K. Wan, J. Arbiol, C. Zhang, S. Liu, M. Xu, X. Zhang and J. Fransaer, *Small*, 2022, **18**, 2103561.
- 69 J.-M. Rueff, M. Poienar, A. Guesdon, C. Martin, A. Maignan and P.-A. Jaffrès, *J. Solid State Chem.*, 2016, **236**, 236–245.
- 70 X. Huang, Q. Dong, H. Huang, L. Yue, Z. Zhu and J. Dai, *J. Nanopart. Res.*, 2014, **16**, 2785.
- 71 Z. Liu, X. Huang, Z. Zhu and J. Dai, *Ceram. Int.*, 2010, **36**, 1155–1158.
- 72 D. Yin, J. Tang, R. Bai, S. Yin, M. Jiang, Z. Kan, H. Li, F. Wang and C. Li, *Nanoscale Res. Lett.*, 2021, **16**, 11.
- 73 I. I. Abu and K. J. Smith, *Catal. Today*, 2007, **125**, 248–255.
- 74 Z. Xing, Q. Liu, A. M. Asiri and X. Sun, *ACS Catal.*, 2015, **5**, 145–149.
- 75 D. C. Phillips, S. J. Sawhill, R. Self and M. E. Bussell, *J. Catal.*, 2002, **207**, 266–273.
- 76 J. R. Hayes, R. H. Bowker, A. F. Gaudette, M. C. Smith, C. E. Moak, C. Y. Nam, T. K. Pratum and M. E. Bussell, *J. Catal.*, 2010, **276**, 249–258.
- 77 Q. Kang, M. Li, J. Shi, Q. Lu and F. Gao, *ACS Appl. Mater. Interfaces*, 2020, **12**, 19447–19456.
- 78 J. A. Cecilia, A. Infantes-Molina, E. Rodríguez-Castellón and A. Jiménez-López, *J. Catal.*, 2009, **263**, 4–15.
- 79 H. Xue, H. Zhang, S. Fricke, M. Lüther, Z. Yang, A. Meng, W. Bremser and Z. Li, *Sustainable Energy Fuels*, 2020, **4**, 1723–1729.
- 80 Z.-Z. Luo, Y. Zhang, C. Zhang, H. T. Tan, Z. Li, A. Abutaha, X.-L. Wu, Q. Xiong, K. A. Khor, K. Hippalgaonkar, J. Xu, H. H. Hng and Q. Yan, *Adv. Energy Mater.*, 2017, **7**, 1601285.
- 81 H. Hou, Q. Peng, S. Zhang, Q. Guo and Y. Xie, *Eur. J. Inorg. Chem.*, 2005, **2005**, 2625–2630.
- 82 B. M. Barry and E. G. Gillan, *Chem. Mater.*, 2008, **20**, 2618–2620.
- 83 H. Kang, T. Lee, Y. Park, Y.-K. Hong, M. Choi, J. Cho and D.-H. Ha, *Korean J. Chem. Eng.*, 2020, **37**, 1419–1426.
- 84 S. Wei, K. Qi, Z. Jin, J. Cao, W. Zheng, H. Chen and X. Cui, *ACS Omega*, 2016, **1**, 1367–1373.
- 85 H. Zhang, D. Shan, Y. Liu, L. Liu, G. Shen, S. Peng, D. Wang and X. Wang, *ACS Appl. Energy Mater.*, 2022, **5**, 10961–10972.
- 86 M. Kim, Y. Park, T. Lee, Y.-k. Hong and D.-H. Ha, *Int. J. Energy Res.*, 2022, **46**, 17668–17681.
- 87 Q. Zhou, L. Liao, Q. Bian, F. Yu, D. Li, J. Zeng, L. Zhang, H. Wang, D. Tang, H. Zhou and Z. Ren, *Small*, 2022, **18**, 2105642.
- 88 D. Shin, H. J. Kim, M. Kim, D. Shin, H. Kim, H. Song and S.-I. Choi, *ACS Catal.*, 2020, **10**, 11665–11673.
- 89 L. Wang, N. Gong, Z. Zhou, W. Peng, Y. Li, F. Zhang and X. Fan, *Int. J. Hydrogen Energy*, 2022, **47**, 18305–18313.
- 90 Y. Gao, S. Qian, H. Wang, W. Yuan, Y. Fan, N. Cheng, H. Xue, T. Jiang and J. Tian, *Appl. Catal., B*, 2023, **320**, 122014.
- 91 Y. Men, P. Li, J. Zhou, S. Chen and W. Luo, *Cell Rep. Phys. Sci.*, 2020, **1**, 100136.
- 92 L. Qian, H. Hu, Y. Zheng, Y. Zhu, Z. Yuan, Y. Dai, T. Zhang, D. Yang and F. Qiu, *Inorg. Chem.*, 2024, **63**, 1682–1691.
- 93 X. Xu, Y. Dong, F. Liu, H. Wang, X. Wang, X. Li, J. Ren and R. Wang, *Int. J. Hydrogen Energy*, 2024, **49**, 984–994.
- 94 T. Zhao, S. Wang, C. Jia, C. Rong, Z. Su, K. Dastafkan, Q. Zhang and C. Zhao, *Small*, 2023, **19**, 2208076.
- 95 D. Xu, J. Yao, X. Ma, Y. Xiao, C. Zhang, W. Lin and H. Gao, *J. Colloid Interface Sci.*, 2022, **619**, 298–306.
- 96 C. Feng, M. Lv, J. Shao, H. Wu, W. Zhou, S. Qi, C. Deng, X. Chai, H. Yang, Q. Hu and C. He, *Adv. Mater.*, 2023, **35**, 2305598.
- 97 G. Barati Darband, M. Maleki, A. Toghraei and S. Shanmugam, *Int. J. Hydrogen Energy*, 2023, **48**, 4253–4263.
- 98 T. Wu, M. Pi, D. Zhang and S. Chen, *J. Mater. Chem. A*, 2016, **4**, 14539–14544.
- 99 Y. Dong, X. Chen, B. Yu, W. Zhang, X. Zhu and Z. Liu, *J. Alloys Compd.*, 2022, **905**, 164023.
- 100 T. A. Shifa, K. Yusupov, G. Solomon, A. Gradone, R. Mazzaro, E. Cattaruzza and A. Vomiero, *ACS Catal.*, 2021, **11**, 4520–4529.
- 101 H. Song, J. Yu, Z. Tang, B. Yang and S. Lu, *Adv. Energy Mater.*, 2022, **12**, 2102573.
- 102 T. Wang, X. Li, Y. Pang, X. Gao, Z. Kou, J. Tang and J. Wang, *Chem. Eng. J.*, 2021, **425**, 131491.
- 103 Y. Li, Y. Wu, H. Hao, M. Yuan, Z. Lv, L. Xu and B. Wei, *Appl. Catal., B*, 2022, **305**, 121033.
- 104 Y. Liu, Z. Zhang, L. Zhang, Y. Xia, H. Wang, H. Liu, S. Ge and J. Yu, *J. Mater. Chem. A*, 2022, **10**, 22125–22134.
- 105 S. Li, L. Wang, H. Su, A. N. Hong, Y. Wang, H. Yang, L. Ge, W. Song, J. Liu, T. Ma, X. Bu and P. Feng, *Adv. Funct. Mater.*, 2022, **32**, 2200733.
- 106 Y. Zhang, N. Li, Z. Zhang, S. Li, M. Cui, L. Ma, H. Zhou, D. Su and S. Zhang, *J. Am. Chem. Soc.*, 2020, **142**, 8490–8497.
- 107 D. Chen, H. Bai, J. Zhu, C. Wu, H. Zhao, D. Wu, J. Jiao, P. Ji and S. Mu, *Adv. Energy Mater.*, 2023, **13**, 2300499.
- 108 X. Lv, S. Wan, T. Mou, X. Han, Y. Zhang, Z. Wang and X. Tao, *Adv. Funct. Mater.*, 2023, **33**, 2205161.
- 109 L. Kumar, B. Antil, A. Kumar, M. R. Das, O. López-Estrada, S. Siahrostami and S. Deka, *ACS Appl. Mater. Interfaces*, 2023, **15**, 54446–54457.
- 110 A. Li, L. Zhang, F. Wang, L. Zhang, L. Li, H. Chen and Z. Wei, *Appl. Catal., B*, 2022, **310**, 121353.
- 111 J. Liu, X. Liu, H. Shi, J. Luo, L. Wang, J. Liang, S. Li, L.-M. Yang, T. Wang, Y. Huang and Q. Li, *Appl. Catal., B*, 2022, **302**, 120862.
- 112 G. Zhang, G. Wang, Y. Liu, H. Liu, J. Qu and J. Li, *J. Am. Chem. Soc.*, 2016, **138**, 14686–14693.
- 113 X. Wang, Z. Na, D. Yin, C. Wang, Y. Wu, G. Huang and L. Wang, *ACS Nano*, 2018, **12**, 12238–12246.
- 114 E. S. Duran-Urbe, A. Sepúlveda-Escribano and E. V. Ramos-Fernandez, *Chem. Eng. J.*, 2023, **474**, 145897.
- 115 Z. Liu, S. Yang, B. Sun, P. Yang, J. Zheng and X. Li, *Angew. Chem., Int. Ed.*, 2020, **59**, 1975–1979.

- 116 D. E. Schipper, Z. Zhao, H. Thirumalai, A. P. Leitner, S. L. Donaldson, A. Kumar, F. Qin, Z. Wang, L. C. Grabow, J. Bao and K. H. Whitmire, *Chem. Mater.*, 2018, **30**, 3588–3598.
- 117 L. Jin, X. Zhang, W. Zhao, S. Chen, Z. Shi, J. Wang, Y. Xie, F. Liang and C. Zhao, *Langmuir*, 2019, **35**, 9161–9168.
- 118 J. Xiao, Z. Zhang, Y. Zhang, Q. Lv, F. Jing, K. Chi and S. Wang, *Nano Energy*, 2018, **51**, 223–230.
- 119 S. Banerjee, A. Kakekhani, R. B. Wexler and A. M. Rappe, *ACS Catal.*, 2023, **13**, 4611–4621.
- 120 Y. Cheng, J. Guo, Y. Huang, Z. Liao and Z. Xiang, *Nano Energy*, 2017, **35**, 115–120.
- 121 G. Li, J. Wang, J. Yu, H. Liu, Q. Cao, J. Du, L. Zhao, J. Jia, H. Liu and W. Zhou, *Appl. Catal., B*, 2020, **261**, 118147.
- 122 T.-Q. Zhang, J. Liu, L.-B. Huang, X.-D. Zhang, Y.-G. Sun, X.-C. Liu, D.-S. Bin, X. Chen, A.-M. Cao, J.-S. Hu and L.-J. Wan, *J. Am. Chem. Soc.*, 2017, **139**, 11248–11253.
- 123 H. Sun, X. Xu, Z. Yan, X. Chen, F. Cheng, P. S. Weiss and J. Chen, *Chem. Mater.*, 2017, **29**, 8539–8547.
- 124 Q. Wang, Z. Zhang, C. Cai, M. Wang, Z. L. Zhao, M. Li, X. Huang, S. Han, H. Zhou, Z. Feng, L. Li, J. Li, H. Xu, J. S. Francisco and M. Gu, *J. Am. Chem. Soc.*, 2021, **143**, 13605–13615.
- 125 Q. Wang, Z. Liu, H. Zhao, H. Huang, H. Jiao and Y. Du, *J. Mater. Chem. A*, 2018, **6**, 18720–18727.
- 126 J. F. Callejas, C. G. Read, C. W. Roske, N. S. Lewis and R. E. Schaak, *Chem. Mater.*, 2016, **28**, 6017–6044.
- 127 A. B. Laursen, K. R. Patraju, M. J. Whitaker, M. Retuerto, T. Sarkar, N. Yao, K. V. Ramanujachary, M. Greenblatt and G. C. Dismukes, *Energy Environ. Sci.*, 2015, **8**, 1027–1034.
- 128 P. He, X.-Y. Yu and X. W. Lou, *Angew. Chem., Int. Ed.*, 2017, **56**, 3897–3900.
- 129 B. Seo, D. S. Baek, Y. J. Sa and S. H. Joo, *CrystEngComm*, 2016, **18**, 6083–6089.
- 130 Y. Li, B. Zhang, W. Wang, X. Shi, J. Zhang, R. Wang, B. He, Q. Wang, J. Jiang, Y. Gong and H. Wang, *Chem. Eng. J.*, 2021, **405**, 126981.
- 131 Y. Zhang, Z. X. Hui, H. Y. Zhou, S. F. Zai, Z. Wen, J. Chen Li, C. C. Yang and Q. Jiang, *Chem. Eng. J.*, 2022, **429**, 132012.
- 132 D. Li, Z. Li, R. Zou, G. Shi, Y. Huang, W. Yang, W. Yang, C. Liu and X. Peng, *Appl. Catal., B*, 2022, **307**, 121170.
- 133 G. Yuan, J. Bai, L. Zhang, X. Chen and L. Ren, *Appl. Catal., B*, 2021, **284**, 119693.
- 134 J. Duan, S. Chen, C. A. Ortíz-Ledón, M. Jaroniec and S.-Z. Qiao, *Angew. Chem., Int. Ed.*, 2020, **59**, 8181–8186.
- 135 L. Yang, L. Huang, Y. Yao and L. Jiao, *Appl. Catal., B*, 2021, **282**, 119584.
- 136 J. Su, L. Jiang, B. Xiao, Z. Liu, H. Wang, Y. Zhu, J. Wang and X. Zhu, *Small*, 2023, 2310317.
- 137 H. Ma, W. Yan, Y. Yu, L. Deng, Z. Hong, L. Song and L. Li, *Nanoscale*, 2023, **15**, 1357–1364.
- 138 L. S. Graves, R. Sarkar, K. U. Lao and I. U. Arachchige, *Chem. Mater.*, 2023, **35**, 6966–6978.
- 139 W.-Z. Zhang, G.-Y. Chen, J. Zhao, J.-C. Liang, L.-F. Sun, G.-F. Liu, B.-W. Ji, X.-Y. Yan and J.-R. Zhang, *J. Colloid Interface Sci.*, 2020, **561**, 638–646.
- 140 X. Zhou, H. Dai, X. Huang, Y. Ren, Q. Wang, W. Wang, W. Huang and X. Dong, *Mater. Today Energy*, 2020, **17**, 100429.
- 141 Y. Pan, K. Sun, Y. Lin, X. Cao, Y. Cheng, S. Liu, L. Zeng, W.-C. Cheong, D. Zhao, K. Wu, Z. Liu, Y. Liu, D. Wang, Q. Peng, C. Chen and Y. Li, *Nano Energy*, 2019, **56**, 411–419.
- 142 G. Cho, Y. Park, H. Kang, Y.-k. Hong, T. Lee and D.-H. Ha, *Appl. Surf. Sci.*, 2020, **510**, 145427.
- 143 J. Zhu, X. Zheng, C. Liu, Y. Lu, Y. Liu, D. Li and D. Jiang, *J. Colloid Interface Sci.*, 2023, **630**, 559–569.
- 144 R. Zhang, J. Huang, G. Chen, W. Chen, C. Song, C. Li and K. Ostrikov, *Appl. Catal., B*, 2019, **254**, 414–423.
- 145 M. A. R. Anjum, M. D. Bhatt, M. H. Lee and J. S. Lee, *Chem. Mater.*, 2018, **30**, 8861–8870.
- 146 C. A. Downes, K. M. Van Allsburg, S. A. Tacey, K. A. Unocic, F. G. Baddour, D. A. Ruddy, N. J. LiBretto, M. M. O'Connor, C. A. Farberow, J. A. Schaidle and S. E. Habas, *Chem. Mater.*, 2022, **34**, 6255–6267.
- 147 J. Xu, J. Li, D. Xiong, B. Zhang, Y. Liu, K.-H. Wu, I. Amorim, W. Li and L. Liu, *Chem. Sci.*, 2018, **9**, 3470–3476.
- 148 J. Staszak-Jirkovský, C. D. Malliakas, P. P. Lopes, N. Danilovic, S. S. Kota, K.-C. Chang, B. Genorio, D. Strmcnik, V. R. Stamenkovic, M. G. Kanatzidis and N. M. Markovic, *Nat. Mater.*, 2016, **15**, 197–203.
- 149 M. Cabán-Acevedo, M. L. Stone, J. R. Schmidt, J. G. Thomas, Q. Ding, H.-C. Chang, M.-L. Tsai, J.-H. He and S. Jin, *Nat. Mater.*, 2015, **14**, 1245–1251.
- 150 J. Yu, Q. Li, Y. Li, C.-Y. Xu, L. Zhen, V. P. Dravid and J. Wu, *Adv. Funct. Mater.*, 2016, **26**, 7644–7651.
- 151 D. Lai, Q. Kang, F. Gao and Q. Lu, *J. Mater. Chem. A*, 2021, **9**, 17913–17922.
- 152 R. Wang, J. Huang, X. Zhang, J. Han, Z. Zhang, T. Gao, L. Xu, S. Liu, P. Xu and B. Song, *ACS Nano*, 2022, **16**, 3593–3603.
- 153 J. Du, S. Liu, Y. Liu, G. Wu, X. Liu, W. Zhang, Y. Zhang, X. Hong, Q. Li and L. Kang, *J. Am. Chem. Soc.*, 2024, **146**, 8464–8471.
- 154 A. A. Saleh, A. Amer, D. M. Sayed and N. K. Allam, *Electrochim. Acta*, 2021, **380**, 138197.
- 155 Y. Tian, Z. Lin, J. Yu, S. Zhao, Q. Liu, J. Liu, R. Chen, Y. Qi, H. Zhang, R. Li, J. Li and J. Wang, *ACS Sustainable Chem. Eng.*, 2019, **7**, 14639–14646.
- 156 Y. Ding, X. Du and X. Zhang, *Appl. Surf. Sci.*, 2021, **543**, 148818.
- 157 H. Lee, H. Jeong, W. Jeong, Y. J. Hwang, B. An, Y. Lee, G. Kim and D.-H. Ha, *Korean J. Chem. Eng.*, 2024, DOI: [10.1007/s11814-024-00249-4](https://doi.org/10.1007/s11814-024-00249-4).
- 158 J. L. Rowell, M. Kang, D. Yoon, K. Z. Jiang, Y. Jia, H. D. Abruña, D. A. Muller and R. D. Robinson, *J. Am. Chem. Soc.*, 2024, **146**, 17613–17617.
- 159 X. Zhao, Z. Xue, W. Chen, Y. Wang and T. Mu, *ChemSusChem*, 2020, **13**, 2038–2042.
- 160 Y. Zhou, L. Gao, H. Chen, H. Wang, J. Zhang, X. Li, F. Duo and G. Guan, *J. Mater. Sci. Technol.*, 2024, **168**, 62–70.